Directional Sensitivity of Cortical Neurons Towards TMS Induced Electric Fields

Konstantin Weise[1,2*+], Torge Worbs[1,3+], Benjamin Kalloch[1,4], Victor H. Souza[5], Aurélien Tristan Jaquier[6], Werner Van Geit[6], Axel Thielscher[3,7], Thomas R. Knösche[1,4]

[1]Methods and Development Group "Brain Networks", Max Planck Institute for Human Cognitive and Brain Sciences, Stephanstr. 1a, 04103 Leipzig, Germany.

[2]Department of Clinical Medicine, Aarhus University, DNK-8200, Aarhus, Denmark

[3]Technical University of Denmark, Magnetic Resonance Section, Department of Health Technology, Kongens Lyngby, Denmark.

[4]Technische Universität Ilmenau, Institute of Biomedical Engineering and Informatics, Gustav-Kirchhoff-Straße 2, 98693 Ilmenau, Germany.

[5]Department of Neuroscience and Biomedical Engineering, Aalto University School of Science, Espoo, Finland

[6]Blue Brain Project, École polytechnique fédérale de Lausanne (EPFL), Biotech Campus, 1202 Geneva, Switzerland

[7]Danish Research Centre for Magnetic Resonance, Section for Functional and Diagnostic Imaging and Research, Copenhagen University Hospital Amager and Hvidovre, Denmark.

* CORRESPONDING AUTHOR

+ contributed equally

Konstantin Weise; Max Planck Institute for Human Cognitive and Brain Sciences, Stephanstr. 1a, 04103 Leipzig, Germany; Technische Universität Ilmenau, Advanced Electromagnetics Group, Helmholtzplatz 2, 98693 Ilmenau, Germany; e-mail: kweise@cbs.mpg.de, phone: +49 341 9940-2580

Abstract

We derived computationally efficient average response models of different types of cortical neurons, which are subject to external electric fields from Transcranial Magnetic Stimulation. We used 24 reconstructions of pyramidal cells (PC) from layer 2/3, 245 small, nested, and large basket cells from layer 4, and 30 PC from layer 5 with different morphologies for deriving average models. With these models, it is possible to efficiently estimate the stimulation thresholds depending on the underlying electric field distribution in the brain, without having to implement and compute complex neuron compartment models. The stimulation thresholds were determined by exposing the neurons to TMS-induced electric fields with different angles, intensities, pulse waveforms, and field decays along the somato-dendritic axis. The derived average response models were verified by reference simulations using a high-resolution realistic head model containing several million neurons. Differences of only 1-2% between the average model and the average response of the reference cells were observed, while the computation time was only a fraction of a second compared to several weeks using the cells. Finally, we compared the model behavior to TMS experiments and observed high correspondence to the orientation sensitivity of motor evoked potentials. The derived models were compared to the classical cortical column cosine model and to simplified ball-and-stick neurons. It was shown that both models oversimplify the complex interplay between the electric field and the neurons and do not adequately represent the directional sensitivity of the different cell types.

The derived models are simple to apply and only require the TMS induced electric field in the brain as input variable. The models and code are available to the general public in open-source repositories for integration into TMS studies to estimate the expected stimulation thresholds for an improved dosing and treatment planning in the future.

1 Introduction

The extension of current models in the area of transcranial brain stimulation beyond the estimation of the electric fields is elementary to improve our understanding of the underlying stimulation processes. The key question is how the electric field modulates the behavior of neuronal structures. Earlier experimental studies showed that the depolarization threshold of isolated straight axons is inversely proportional to the cosine of the angle between the external current and the nerve fiber (Rushton, 1927). This led to the well known cortical column cosine hypothesis (Fox et al., 2004), assuming that excitable neuronal elements, in particular axons, have a preferential orientation perpendicular to the cortical surface. At first glance, this model seems to be supported by the findings of Rudin and Eisenman (1954) and Ranck (1975), who consistently found that orthodromic currents are more effective than antidromic currents and especially transverse currents. Note, however, that the complex morphology of the neurons does not allow the generalization of observations made in single isolated axons to neuronal populations, because the orientations of the axon segments relative to the external electric field vary and have to be considered statistically. Accounting for these effects requires a model description across multiple scales. This involves first determining the electric field in the brain by solving Maxwell's equations and then coupling it with detailed mesoscopic neuron models. Aberra et al. (2022) introduced a novel approach to simulate the effects of TMS in head models with morphologically realistic cortical neurons. These authors developed a multi-scale computational model that is capable of quantifying effects of different TMS parameters on the direct response of individual cortical neurons. They created digital representations of neurons that match the geometry and biophysical properties of mature human neocortical cells based on neuronal models of rodent cells from the Blue Brain Project (Markram et al. 2015). These models included a spatial representation of the neuronal compartments as well as experimentally validated electrophysiological parameters (Aberra et al., 2018). They were placed inside the gray matter of a realistic head model and the stimulation thresholds for the generation of action potentials were determined by coupling them with the TMS induced electric fields. The results provide important mechanistic insights into TMS. However,

74   a major limitation of this modeling approach is its high computational cost, which prevents most

75   routine applications of the method in TMS studies. Moreover, a further challenge is that for estimating

76   the overall threshold of a cortical group of neurons, the results of a large number of single simulated

77   responses need to be determined and averaged. This calls for the development of simpler models of

78   neural populations that still accurately account for the modulation of neuronal states through TMS-

79   induced electric fields.

80   We developed a parsimonious model, which reproduces the effect of the electric field on cortical

81   neurons with high accuracy for different pulse waveforms and geometric electric field parameters. We

82   adapted and extended the approach of Aberra et al. (2020) to derive an average threshold model of

83   layer 2/3 pyramidal cells (L2/3 PC), small, nested, and large basket cells in layer 4 (L4 SBC, L4 NBC, L4

84   LBC), and layer 5 pyramidal cells (L5 PC). We adapted the pipeline of Aberra et al (2020) in Python and

85   implemented additional improvements and extensions, such as support for SimNIBS 4 and the CHARM

86   head modeling pipeline (Puonti et al. 2020). The code and associated example scripts are published in

87   the open-source Python package *TMS-Neuro-Sim* (https://github.com/TorgeW/TMS-Neuro-Sim).

88   Additionally, we determined estimators for the neuronal recruitment rate, which quantifies the

89   relative number of neurons stimulated by TMS at a given stimulation intensity and field orientation.

90   To further investigate the derived models, we performed a sensitivity analysis and identified the most

91   influential parameters of the models by determining so-called Sobol indices using a generalized

92   polynomial chaos expansion (Weise et al., 2020b) . Moreover, the model was verified by comparing it

93   to results of computationally expensive reference simulations, using a high resolution realistic head

94   model with a large number of realistically shaped neurons located within the motor cortex. Finally, we

95   validated the model by comparing it with TMS experiments by Souza et al. (2022), who intensively

96   investigated the directional sensitivity of motor evoked potentials using a novel multi-coil TMS

97   transducer.

4

98   We also compared the results with those of the cortical column cosine (Fox et al., 2004) as well as a

99   simplified ball-and-stick model (Bédard and Destexhe, 2008) adapted for TMS. It turned out that the

100   stimulation properties differ significantly from detailed neurons and that a simplified modeling

101   strategy is not appropriate in this context.

102   All data and code underlying the results presented in this paper, together with additional details

103   including the average threshold models, the recruitment rate operators, and the neuron compartment

104   models, are publically available in a repository (Weise et al., 2023b), where we provide look-up tables,

105   interpolators, and polynomial approximations for further use.

2 Methods

2.1 Neuron models

108   To derive the average neuron response models, we extended the set of neural compartment models

109   by Aberra et al. (2020) from originally five neurons to 24 L2/3 PC, 70 L4 SBC, 70 L4 NBC, 105 L4 LBC,

110   and 30 L5 thick-tufted pyramidal cells (TTPC's), taken from the Blue Brain Project (Ramaswamy et al.,

111   2015). The cells originate from the somatosensory cortices of P14 male Wistar (Han) rats (Markram et

112   al., 2015). They were stained with biocytin, visually recorded with a bright-field light microscope, and

113   processed by the software Neurolucida (Williston, VT, USA). Shrinkage due to staining in the *z*-axis was

114   corrected during the reconstruction. In an unraveling step, shrinkage in the *xy*-axis was corrected for

115   with a method based on the centered moving window algorithm by smoothing and extending the reach

116   of the branches while maintaining their overall length (Anwar et al., 2009). For branch repair, the

117   cutting planes were first determined and the cut branches were then statistically regrown based on

118   the intact branches. Because some resulting cell morphologies contain impoverished axonal/dendrite

119   branching, a mix-and-match procedure was used to create cells with valid dendrite and axonal

120   reconstructions. As a last step to increase morphological diversity, a cloning procedure was applied.

121   The procedure assigns distributions to branch length and rotation while preserving the overall

122   branching structure.

123   Because the cells provided were from rats, further modifications were necessary to obtain human-like

124   neurons. We followed the procedure and parameters given in Aberra et al. (2018) to extend the set of

125   neurons. First, the basal dendritic diameter, basal dendritic length, apical dendritic diameter, somatic

126   diameter, and axonal diameter were scaled to create adult human-like neuron morphologies. Second,

127   the axons were myelinated by registering nodes of Ranvier with a width of 1 μm, creating myelinated

128   sections with a length (L) to diameter (D) ratio of L/D=100 and myelinated axon terminals with L/D=70

129   (Hursh 1939, Hess and Young 1949, Waxman and Kocsis 1995). And third, the ion channel properties

130   were adapted according to the myelination (see Table 1 in Aberra et al., 2018). Fig. 1 provides an

131   overview of the cells used in the study. The average numbers of nodes per cell are 3,541 for L2/3 PC,

132   14,779 for L4 SBC, 13,091 for L4 NBC, 9,147 for L4 LBC, and 12,514 for L5 PC. For the compartment

133   models, the neurons were discretized with a maximum compartment length of 20 µm. This resulted in

134   an average number of compartments of 766 for L2/3 PC, 1,447 for L4 SBC, 1,762 for L4 NBC, 1,876 for
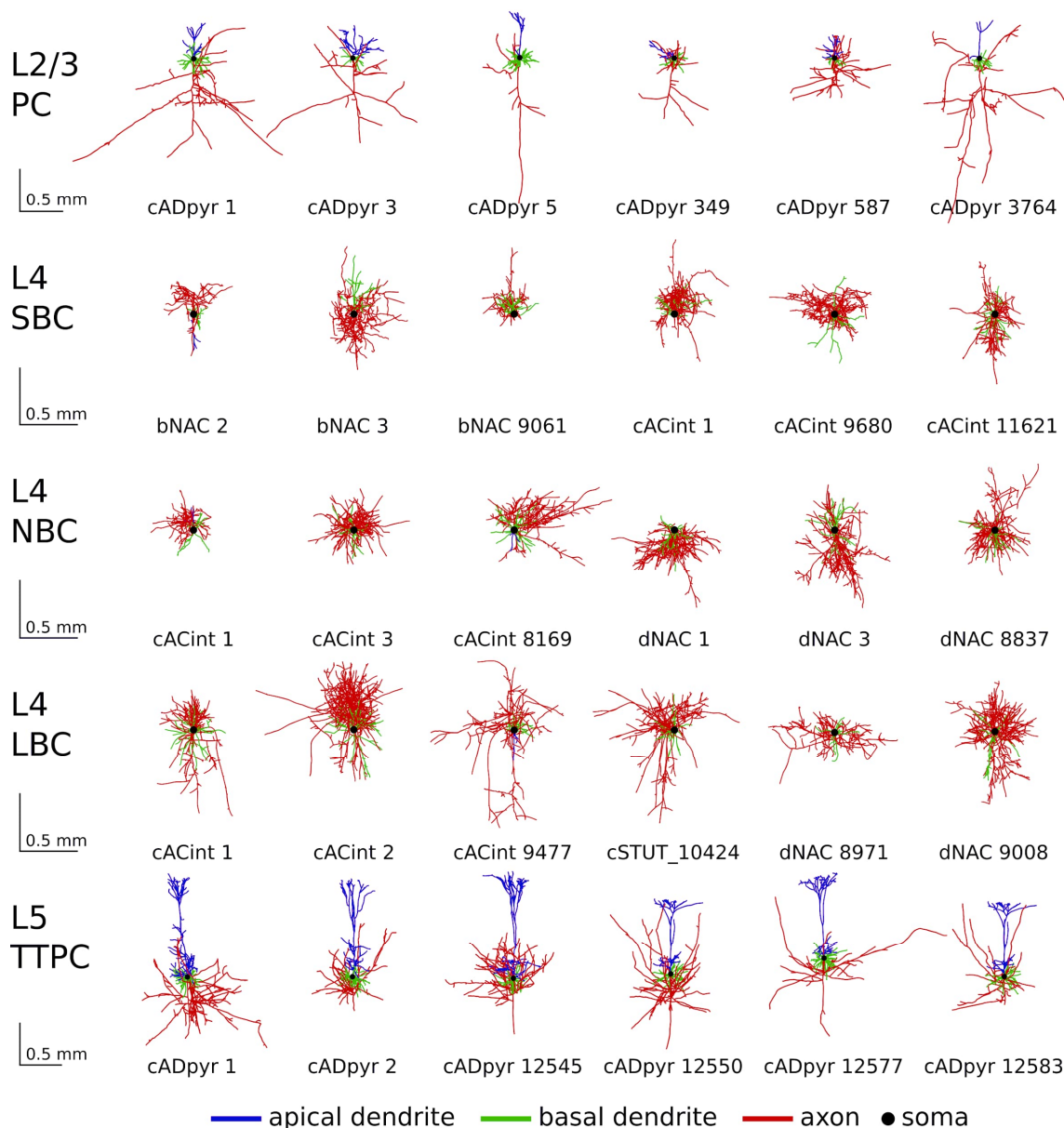
135   L4 LBC, and 2,008 for L5 PC.

Figure 1: Example morphologies of L2/3 PC, L4 S/N/LBC, and L5 PC: The numbers below the cells indicate the corresponding IDs in the repository Weise et al. (2023b). L4 BC are categorized in small basket cells (SBC), nested basket cells (NBC), and large basket cells (LBC). In total, the study includes 24 L2/3 PC, 70 L4 SBC, 70 L4 NBC, 105 L4 LBC, and 30 L5 thick-tufted pyramidal cells (TTPC's), taken from the Blue Brain Project (Ramaswamy et al., 2015).

2.2 Coupling of electric fields into neuron models

The electric field E(z, t) caused by TMS generates an additional extracellular pseudo-potential φ_e(z, t). It is coupled into the neurons' cable equations by integrating the electric field component along the local longitudinal direction dz of each neuronal compartment, ranging from, for example, the initial point of a compartment z_0 to the end of that compartment z:

7

$$\varphi_e(z,t) = -\int_{z_0}^{z} \mathbf{E}(z,t) \cdot \mathbf{dz} + \varphi_e(z_0,t)$$

148

(1)

149   For the realistic head model simulations, the electric field is interpolated to the neurons' segments

150   using the superconvergent patch recovery approach (Zienkiewicz and Zhu, 1992).

151   ## 2.3 Neuronal simulations

152   The stimulation behavior of the neurons is analyzed by calculating the transmembrane potential in

153   each compartment using NEURON (Carnevale and Hines, 2006) following a similar approach as Aberra

154   et al. (2020). The spatio-temporal dynamics of the transmembrane potential were modeled according

155   to the Hodgkin-Huxley formalism. Detailed information about the ion channel parameters and

156   membrane time constants can be found in the repository by Weise et al. (2023b) and ModelDB

157   (https://senselab.med.yale.edu/modeldb/ShowModel.cshtml?model=241165) by Aberra et al. (2018).

158   The NEURON simulation was set up with a temperature of 37° C and an initial voltage of -70 mV for

159   each compartment. The simulations were carried out over the course of 1 ms with time steps of 5 μs.

160   The extracellular quasipotentials were scaled by the waveform and the amplitude of the TMS pulse.

161   The used monophasic and biphasic waveforms were taken from a MagPro X100 stimulator

162   (MagVenture A/S, Denmark) with a MagVenture MCF-B70 figure-of-eight coil (P/N 9016E0564) and

163   were recorded using a search coil with a sampling rate of 5 MHz. The recordings were down-sampled

164   to the simulation time steps and normalized to be applicable for scaling the extracellular potential. The

165   cell thresholds are determined as the minimum electric field intensity needed to elicit action potentials

166   in at least three compartments, using a binary search approach with a precision of 0.05 V/m. The

167   simulation environment is implemented and published in the open-source Python package *TMS-*

168   *Neuro-Sim* (https://github.com/TorgeW/TMS-Neuro-Sim) making use of the Python API of NEURON.

169   The example dataset (Weise et al., 2023b) contains the neuron models together with example scripts

170   detailing the use of the implemented functions.

171   2.4 Average response model of cortical neurons

172   We exposed the model neurons to electric fields from different directions and strengths to examine

173   their stimulation behavior in detail. We parameterized the electric field direction using spherical

174   coordinates (Fig. 2a). The polar angle ϑ quantifies the angle between the electric field and the somato-

175   dendritic axis (z-axis) and ranges from 0° to 180°. The azimuthal angle φ quantifies the electric field

176   direction in the horizontal plane perpendicular to the somato-dendritic axis and ranges between 0°

177   and 360°. The coordinate system is defined such that the soma is lying close to the center and the axon

178   extends into negative z-direction. Because of the comparatively large extension of the PC from the

179   uppermost dendrites to the lowermost part of the axon, the decay of the electric field along the z-axis

180   is not negligible. In simulations of a realistic head model, we found that the electric field can differ up

181   to ±20% per mm over the somato-dendritic axis. A more detailed analysis of the underlying parameter

182   distributions is given later in Section "Sensitivity analysis". For this reason, we have added an additional

183   parameter to the model, namely the relative change of the electric field magnitude per unit length

184    $\Delta|\tilde{\mathbf{E}}|$ measured in %/mm.

185   The electric field at each location (x, y, z) at firing threshold is then given by:

$$\mathbf{E}\left(z, \varphi, \theta, \Delta\left|\tilde{\mathbf{E}}\right|\right) = E_{thres} \begin{pmatrix} \sin\theta\cos\varphi \\ \sin\theta\sin\varphi \\ \cos\theta \end{pmatrix} \max\left(\frac{\Delta\left|\tilde{\mathbf{E}}\right|}{100}(z - z_{soma}) + 1\right)$$

186   (2)

187   where z_{soma} is the position of the soma on the z-axis (in mm). The soma will have an electric field

188   magnitude of E_{thres}, which is to be found using the aforementioned binary search approach, while the

189   magnitude for every other section of the cell is linearly interpolated based on their z-coordinate. An

190   example of an external electric field distribution with φ=0°, ϑ=135° and $\Delta|\tilde{\mathbf{E}}|$=−30%/mm is shown in

191   Fig. 2b.

192   For the derivation of an average response model, all L2/3 and L5 neurons were exposed to an external

193   electric field with a polar angle ϑ (range: [0, 180]°, steps: 3°), an azimuthal angle φ (range: [0, 360]°,

194   steps: 6°), and a relative change of the electric field along the somato-dendritic axis $\Delta|\tilde{\mathbf{E}}|$ (range: [-100,

195   100] %/mm, steps: 10 %/mm) for both monophasic and biphasic pulse waveforms. After determining

196   the electric field thresholds for each cell for all possible electrical field configurations, an average

197   threshold model was derived by averaging the thresholds over all compartment models and over all

198   azimuthal orientations φ, based on the assumption that the spatial locations and tangential

199   orientations of the neurons in the cortex are random.

200   From the activation thresholds of the individual neurons, we determined the recruitment rate of the

201   neurons in dependence of ϑ and $\Delta|\tilde{\mathbf{E}}|$. The recruitment rate estimates the relative number of neurons

202   which were stimulated by TMS at a given stimulation intensity, with zero corresponding to no

203   stimulation and one corresponding to stimulation of all neurons. To this end, we integrated the electric

204   field thresholds along the electric field axis and smoothed the discrete behavior by fitting continuous

205   sigmoid functions of the following type in the least squares sense:

$$f(E) = \left(1 + e^{-r\left(\theta,\, \Delta|\tilde{\mathbf{E}}|\right)\left(E - E_0\left(\theta,\, \Delta|\tilde{\mathbf{E}}|\right)\right)} \right)^{-1}$$

206   (3)

207   where E denotes the electric field, $r(\theta, \Delta|\tilde{\mathbf{E}}|)$ the slope, and $E_0(\theta, \Delta|\tilde{\mathbf{E}}|)$ the shift of the sigmoidal

208   functions, which depend on both the polar angle ϑ and the relative change in electric field $\Delta|\tilde{\mathbf{E}}|$.

209   A threshold model was also created for a simplified ball-and-stick neuron model. Typically, ball-and-

210   stick models are used for stimulation by weak electric fields in the context of transcranial electric

211   stimulation (e.g., Aspart et al., 2016) and consist of one segment for the dendrites and one segment

212   for the soma. Because the stimulation thresholds for TMS-induced electric fields of the dendrites are

213   more than 10 times higher than those of the axons, the classical ball-and-stick model had to be

214   modified for TMS. For this purpose, we integrated a straight axon instead of dendrites into the model

215   and determined the stimulation thresholds as a function of the polar angle θ using the approach

216   described by Aberra at al. (2020). For a similar approach, see also the supplementary material of that

217   article). The parameters (axon length and diameter) were adapted such that the thresholds matched
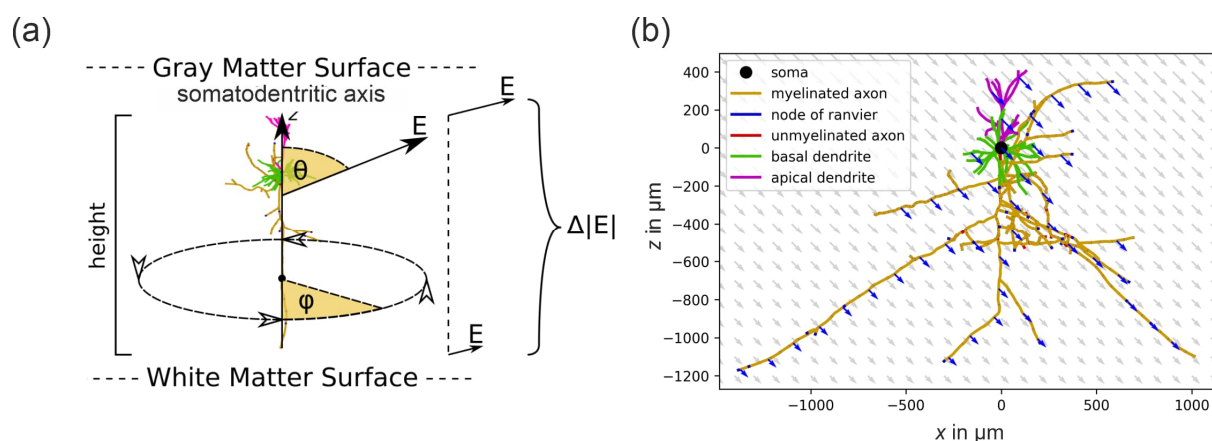
218   those of our complex model.

Figure 2: Neurons in an external electric field: (a) Parametrization of the TMS induced electric field relative to cortical neurons; (b) Example of an L2/3 PC, which is exposed to an external electric field with direction φ=0°, ϑ=135° and a field decay of $\Delta|\tilde{E}|$=−30%/mm. Note that the electric field is stronger in the upper part of the cell and decreases with depth, as is generally observed in the cortex.

2.5 Sensitivity analysis

A sensitivity analysis of the derived threshold maps was conducted in terms of variations of the electric field parameters θ and $\Delta|\tilde{E}|$. We derived a generalized polynomial chaos expansion of the threshold maps using the Python package *pygpc* (Weise et al., 2020b) and determined the first- and second-order Sobol indices that quantify the fraction of the total variance of the threshold that stems from the variance of θ, from the variance of $\Delta|\tilde{E}|$, and from a combination of both. The input distributions of both parameters were estimated from the electric field simulation of the high-resolution realistic head model. We extracted the polar angles θ and the changes in electric field magnitude $\Delta|\tilde{E}|$ in every surface element of layer 5 in the ROI and fitted uniform and beta distributions to the histograms (Fig. 3). We repeated the analysis for layer 2/3 and layer 4, and did not find any major differences in the parameter distributions, due to the close proximity of the layers. For the uncertainty analysis we assumed that both parameters are uncorrelated.
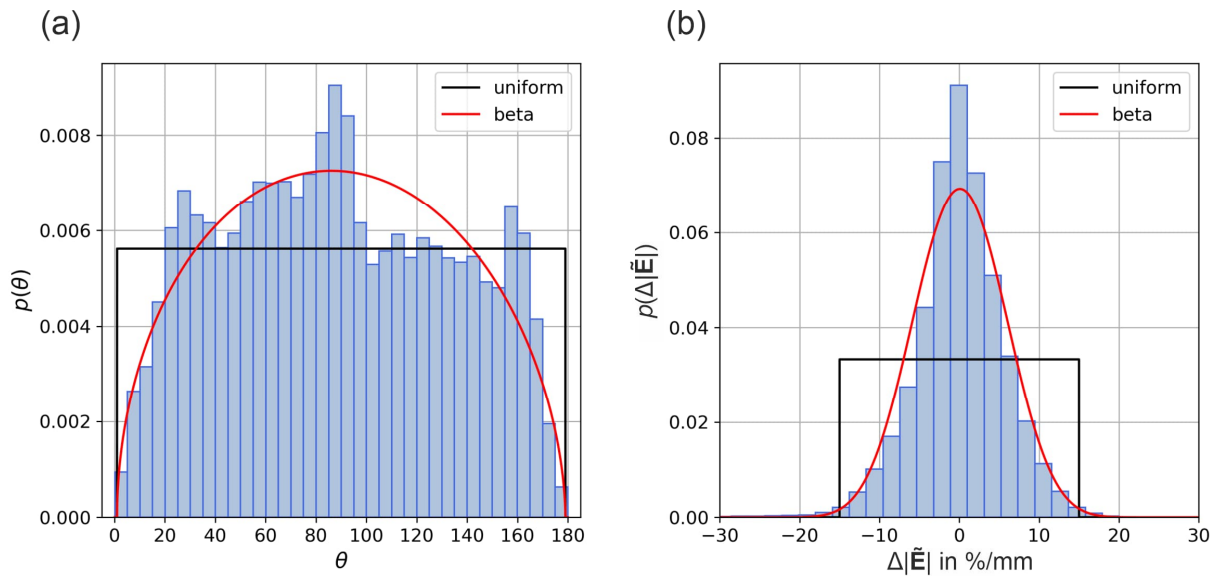
(a)
(b)

Figure 3: Distribution of electric field parameters on layer 5 in a realistic head model: Histograms and fitted uniform and beta distributions of (a) the polar angle ϑ (uniform parameters: $\vartheta_{min}=0°$, $\vartheta_{max}=180°$; beta parameters: $\vartheta_{min}=0°$, $\vartheta_{max}=180°$; $p=1.51$, $q=1.56$) and (b) the relative change of the electric field magnitude $\Delta|\tilde{E}|$ (uniform parameters: $\Delta|\tilde{E}|_{min}=-15°$, $\Delta|\tilde{E}|_{max}=15°$; beta parameters: $\Delta|\tilde{E}|_{min}=-30°$, $\Delta|\tilde{E}|_{max}=30°$; $p=13.86$, $q=13.78$).

2.6 Model verification

In order to verify the average response model, we conducted reference simulations using a high resolution realistic head model, where we explicitly placed the neurons in the ROI and coupled the TMS-induced electric field into them. The head model was created using T1-, T2-, and diffusion weighted MRI. The images were acquired on a 3T MRI scanner (Siemens Skyra) with a 32 channel head coil using the same acquisition parameters as described in Weise et al. (2023a). T1 and T2 images were used for tissue type segmentation. Conductivity tensors in gray and white matter were reconstructed from diffusion weighted images using the volume normalized mapping approach (dwi2cond, https://simnibs.github.io/simnibs/build/html/documentation/command_line/dwi2cond.html, Güllmar et al., 2010). The head model was generated using the headreco pipeline (Nielsen et al., 2018) utilizing SPM12 (https://www.fil.ion.ucl.ac.uk/spm/software/spm12/, Penny et al., 2011) and CAT12 (http://www.neuro.uni-jena.de/cat/, Gaser et al., 2021). A region of interest (ROI) was defined around the handknob area (FreeSurfer, (http://surfer.nmr.mgh.harvard.edu/, Fischl et al., 1998; Dale et al., 1999) based on the fsaverage template. This covered parts of somatosensory cortex (BA1, BA3),

12

256   primary motor cortex M1 (BA4), and dorsal premotor cortex PMd (BA6). The head model was refined

257   in the ROI to provide accurate electric field values for the neuron models (Fig. 4). The final head model

258   is composed of ~$5\cdot10^6$ nodes and ~$29\cdot10^6$ tetrahedra. The tetrahedra in the ROI have an average edge

259   length of 0.45 mm and an average volume of 0.01 mm³. The model consists of six tissue types with the

260   following electrical conductivities: white matter (0.126 S/m), grey matter (0.275 S/m), cerebrospinal

261   fluid (1.654 S/m), bone (0.01 S/m), skin (0.465 S/m), and eyeballs (0.5 S/m) (Thielscher et al., 2015;

262   Wagner et al., 2004). The entire process from MRI acquisition to the final head model can be

263   reproduced in detail using the protocol of Weise et al. (2023a) (steps 1-20) and details of the FEM are

264   given in Saturnino et al. (2019).

265   In order to place the neurons at the right locations in the cortex , we added cortical layers to the head

266   model. The normalized depths of the six cortical layers range between 0 (gray matter surface, i.e. pia

267   mater) and 1 (white matter surface) and were estimated from primate motor cortex slices (García-

268   Cabezas et al., 2014). The normalized depths of the layer centers are 0.06 for layer 1, 0.4 for layer 2/3,

269   0.55 for layer 4, 0.65 for layer 5, and 0.85 for layer 6 (Aberra et al., 2020). We linearly interpolated

270   between the white matter surface (1) and the gray matter surface (0) using the vertex positions of the

271   two surfaces. To extract the cortical layers as isosurfaces from the 3D interpolation, we used a

272   marching cubes algorithm (Fig. 3) (Lorensen et al., 1987). In every ROI surface element (size ~1 mm²),

273   we placed all cells and rotated them from 0° to 360° in steps of 6°. This resulted in a total number of

274   12,947,040 L2/3 PC, 130,080,300 L4 S/N/LBC, and 15,760,800 L5 PC in the ROI to simulate. The total

275   pure simulation time using 48 cluster nodes with 72 cores each (Intel Xeon Platinum 8360Y, 256 GB

276   RAM) was approximately 40 days for both monophasic and biphasic waveforms.

277   The electric field calculations were conducted using SimNIBS v3.2.6 (Thielscher et al, 2015; Saturnino

278   et al., 2019) using a regular figure-of-eight coil (MCF-B65, Magventure, Farum, Denmark), which is

279   placed over the M1 region with an orientation of 45° towards the *fissura longitudinalis*. The angle ϑ of

280   the electric field was calculated with respect to the surface normal of the cortical layers in the ROI.

281   Likewise, the percentage change of the electric field magnitude between the WM and GM surfaces

13

282 $\Delta|\tilde{E}|$ was calculated by extracting the field at a normalized depth of 10 % of the distance between the

283 current layer and the WM and GM surface, respectively, in order to avoid numerical inaccuracies close

284 to the tissue boundaries. The simulation time of the electric field was relatively short compared to the
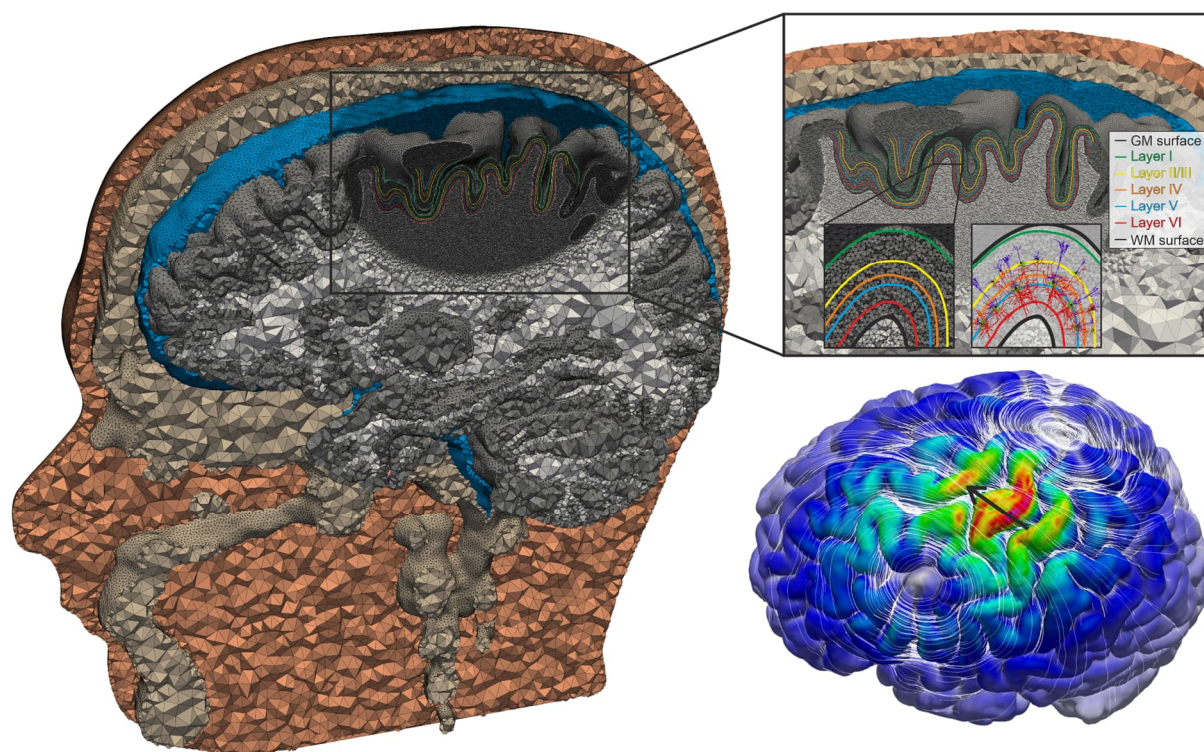
285 NEURON simulations and took a few seconds.

286

287 Figure 4: Realistic head model with cortical layers and neurons: The model was constructed with
288 SimNIBS v3.2.6 (Thielscher et al. 2015) using *headreco* (Nielsen et al., 2018). In the M1 region, the
289 cortical layers 1-6 are generated and the mesh is refined to ensure highly accurate electric field
290 profiles, which are coupled into the compartment models of cortical neurons. The bottom right inset
291 shows an example of the magnitude of the electric field as color code and its orientation as white
292 streamlines. The black arrow indicates the coil orientation.

293 2.7 Experimental validation

294 We compared the derived recruitment models to experimental observations from Souza et al. (2022).

295 TMS experiments were conducted to investigate the orientation selectivity of neuronal excitability

296 using a novel two-coil multi-channel TMS transducer for manipulating the electric field orientation.

297 The advantage of the used two-coil TMS transducer is the possibility to precisely manipulate the pulse

298 orientation electronically with high accuracy (~1°), without physically moving the transducer. To

299 measure the effect of the electric field orientation on the motor evoked potential (MEP) amplitude,

300 five single TMS pulses were applied to the *abductor pollicis brevis* (APB) muscle hotspot at each of 120

301 different pulse orientations (0–360°; steps of 3°) with a stimulation intensity of 110% of the resting

302 motor threshold (rMT). The MEPs from the APB muscle were recorded from 11 subjects (mean age: 30

303 years, range 24-41; four women) using surface electromyography electrodes with a belly-tendon

304 montage. TMS pulses had a trapezoidal monophasic waveform (timings: 60 μs of rising, 30 μs of hold,

305 43.2 μs of falling) and were delivered using a custom power electronics. The interstimulus intervals

306 were pseudo-randomized following a uniform distribution between 4 and 6 s. In two other subjects

307 (ages 31 and 36 years; two men; right-handed), the experiment was repeated with stimulation

308 intensities of 110%, 120%, 140%, and 160% rMT. The order of the orientations and intensities of the

309 pulses was pseudo-randomized. A detailed description of the experimental procedure and TMS

310 hardware is given in Souza et al. (2022).

3 Results

311

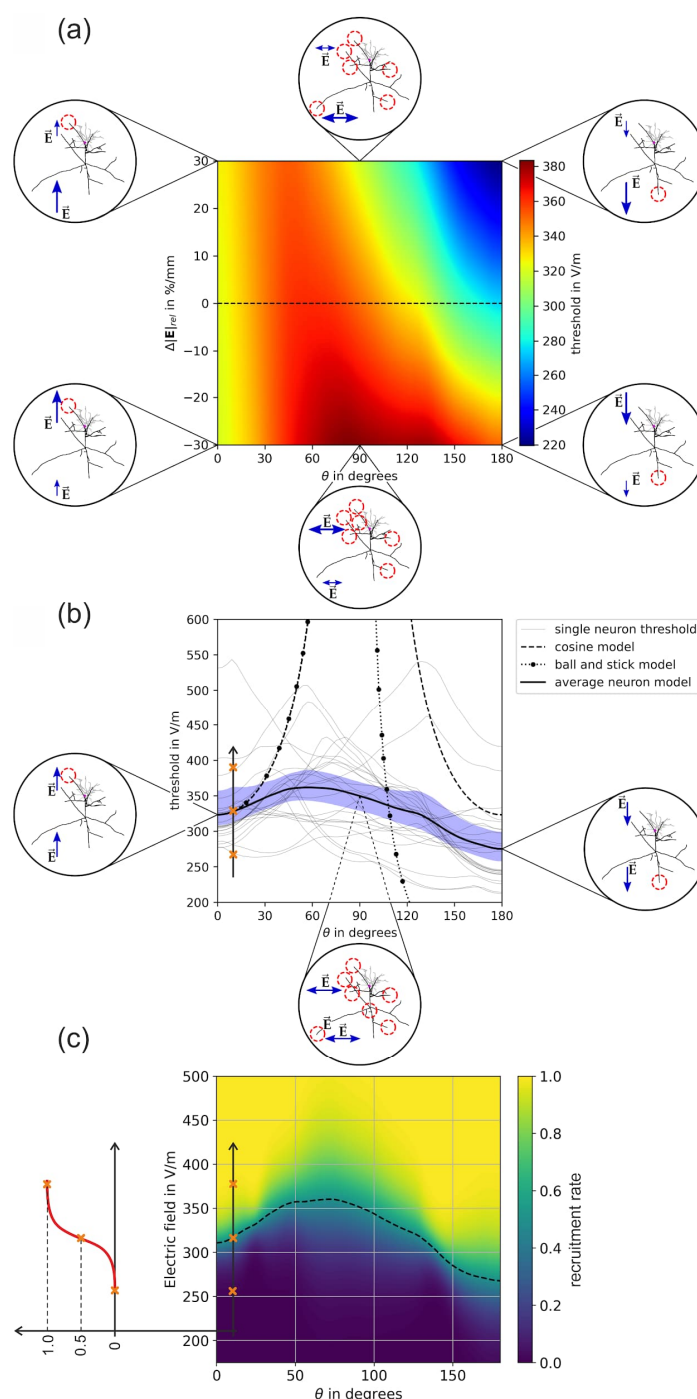## 3.1 Stimulation behavior of L2/3 PCs

312

313 The results of the average response model of L2/3 PCs in case of a monophasic TMS pulse is shown in

314 Fig. 5. In Fig. 5a, the electric field thresholds are shown as function of the polar angle ϑ and the relative

315 change in electric field magnitude $\Delta|\tilde{E}|$. For parameter combinations of particular interest, we

316 illustrated the stimulation location on a representative neuron. Lowest thresholds can be observed

317 when the electric field is parallel to the somato-dendritic axis. This effect is enhanced for positive

318 electric field changes, that is, when the electric field increases from the dendrites to the lower parts of

319 the axons.

320 The behavior of the 24 individual L2/3 neurons is shown in Fig. 5b for homogeneous electric fields, i.e.,

321 $\Delta|\tilde{E}|=0$ %/mm (dashed line in Fig. 5a). It can be observed that the electric field thresholds are highest

322 when the electric field is approximately normal to the somato-dendritic axis ($\vartheta \approx 90°$). Since in this case

15

323   the electric field can approach from all azimuthal directions φ over which the average was taken, there

324   are several potential stimulation sites. The thresholds are decreasing again when the electric field

325   rotates further until it is pointing antidromic, i.e. from the axons to the dendrites (ϑ=0°). In this case

326   the activation takes place at cortico-cortical axon branches pointing upwards. This effect is stable in

327   terms of electric field changes along the somato-dendritic axis. It is noted that due to the geometrical

328   relations of the two electric field angles ϑ and φ, the more parallel the electric field is to the somato-

329   dendritic axis ($\vartheta \rightarrow$0°, $\vartheta \rightarrow$180°) the less the azimuthal direction φ plays a role on the stimulation

330   behavior of the neurons. The thresholds for tangential electric fields (ϑ=90°) are about 17% higher

331   compared to normal electric fields (ϑ=0° and ϑ=180°). The recruitment rates are shown in Fig. 5c for

332   homogeneous electric fields, i.e. $\Delta|\tilde{\mathbf{E}}|$=0 %/mm.

333   We provide the data of the threshold map from Fig. 5a, the individual neuron behavior from Fig. 5b

334   and beyond, as well as the data of the recruitment rate from Fig. 5c in the associated dataset (Weise

335   et al. 2023b). In addition, we provide Python based SciPy interpolators (Virtanen et al., 2020), whose

336   simple usage is also explained in attached scripts.

337   The results for biphasic excitation are shown in Fig S1 in the *Supplemental Material.*

Figure 5: Stimulation behavior of L2/3 PCs for monophasic excitation: (a) Threshold map in dependence of the polar angle ϑ and the relative change of the electric field over the somato-dendritic axis $\Delta|\tilde{\mathbf{E}}|$. The insets show the locations of excitation, the red circles indicate the activated terminals. Blue arrows indicate the electric field direction and magnitude; (b) Thresholds of individual neurons for $\Delta|\tilde{\mathbf{E}}|$=0 %/mm along the dashed line in (a). The blue area shows the 95th percentile of the confidence interval of the mean. The equivalent cortical column cosine model is $y(\theta) = \hat{y}|\cos(\theta)|^{-1}$ with ŷ=323.27 V/m (dashed line); ; the axon parameters of the equivalent ball-and-stick model are $l = 660\,\mu\mathrm{m}$ and $d = 15\,\mu\mathrm{m}$ (dotted line); (c) Recruitment rate for $\Delta|\tilde{\mathbf{E}}|$=0 %/mm derived from the individual neuron activation in (b) by integrating over the electric field thresholds. The dashed line indicates the electric field intensity where the recruitment rate is 0.5.

17

349   3.2 Stimulation behavior of L4 BCs

350   3.2.1 Small Basket cells

351   The results of the average response model of L4 SBCs in case of a monophasic excitation is shown in

352   Fig. 6. A pronounced directional sensitivity can be observed also for this cell type. Again, lowest

353   thresholds can be observed when the electric field is parallel to the somato-dendritic axis (ϑ=0° and

354   ϑ=180°). The thresholds are about 17% higher when the external electric field is tangential to the cells

355   (ϑ=90°). The thresholds are slightly affected if the electric field changes along the somato-dendritic

356   axis ($\Delta|\tilde{\mathbf{E}}| \lesssim 0$ %/mm). Compared to other cells, the average threshold is about 20% and 46% higher for

357   L4 SBCs than for L2/3 PCs and L5 PCs, respectively. The results for biphasic excitation are shown in Fig
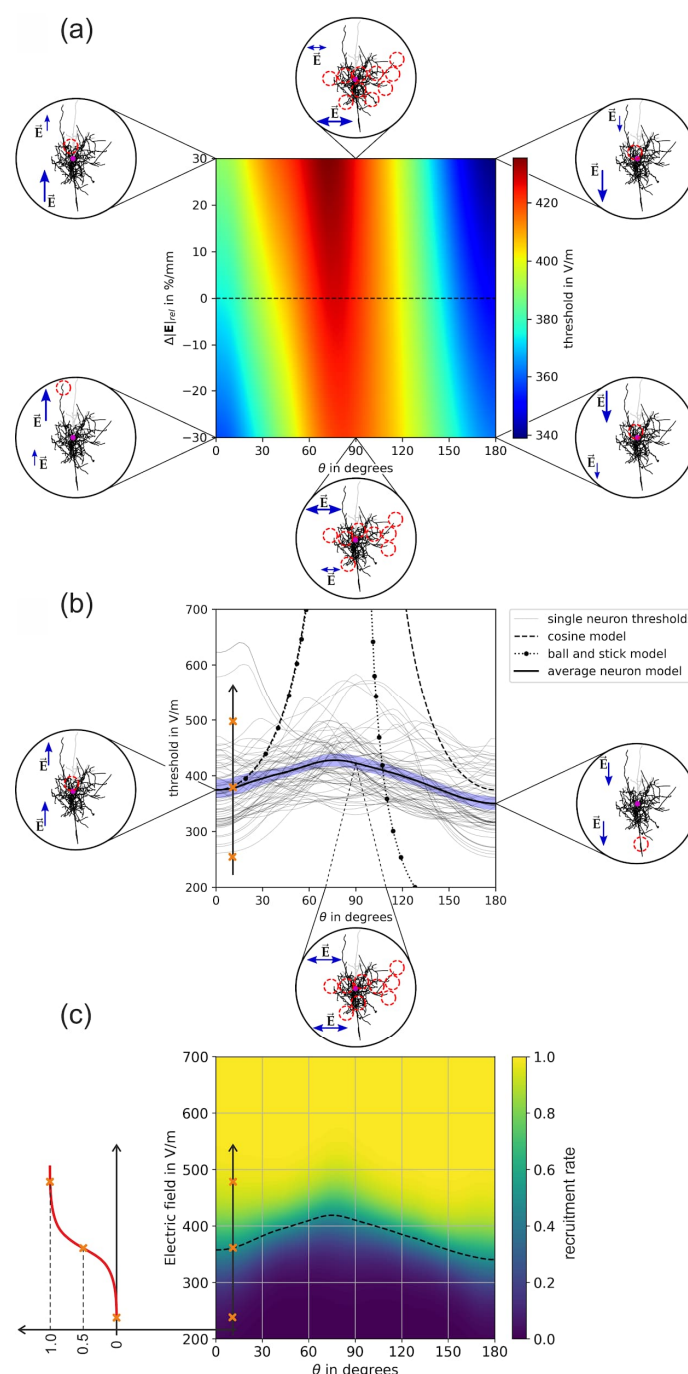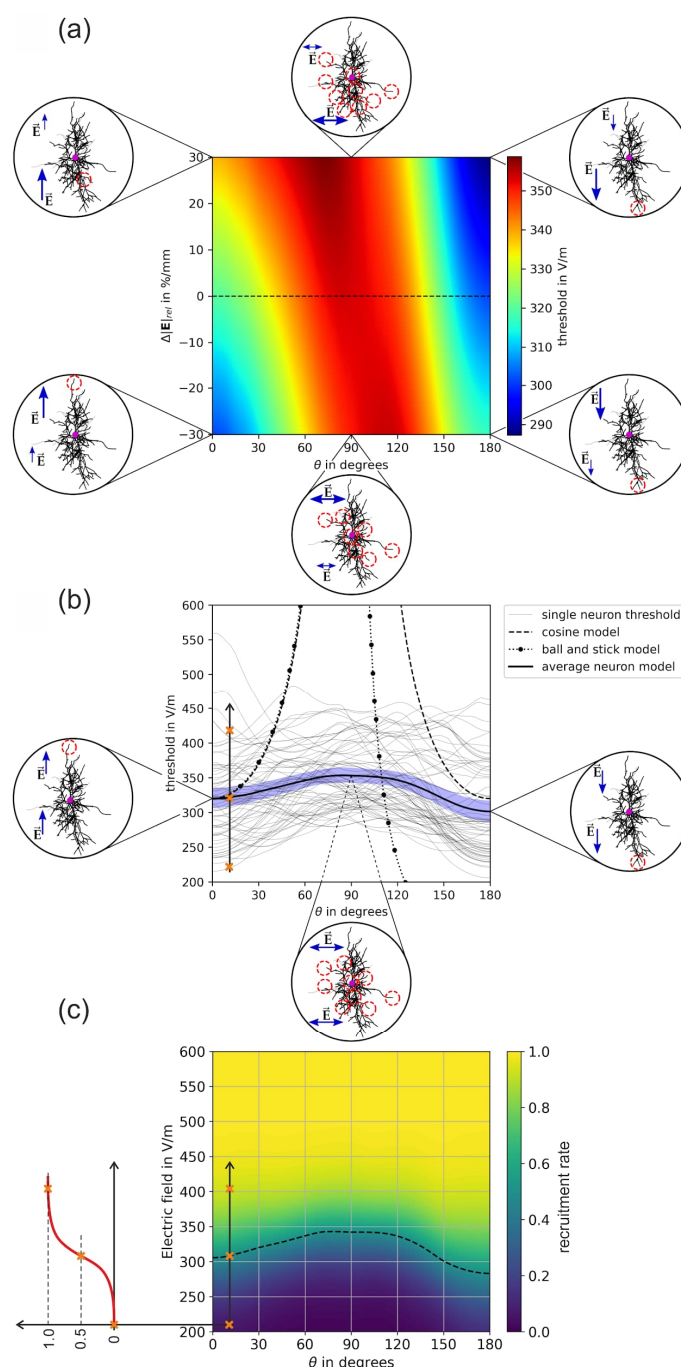
358   S2 in the *Supplemental Material.*

Figure 6: Stimulation behavior of L4 SBCs for monophasic excitation: (a) Threshold map in dependence of the polar angle ϑ and the relative change of the electric field over the somato-dendritic axis $\Delta|\tilde{\mathbf{E}}|$. The insets show the locations of excitation, the red circles indicate the activated terminals. Blue arrows indicate the electric field direction and magnitude; (b) Thresholds of individual neurons for $\Delta|\tilde{\mathbf{E}}|$=0 %/mm along the dashed line in (a). The blue area shows the 95th percentile of the confidence interval of the mean. The equivalent cortical column cosine model is $y(\theta) = \hat{y}|\cos(\theta)|^{-1}$ with ŷ=178.43 V/m (dashed line); the axon parameters of the equivalent ball-and-stick model are $l = 440\,\mu\mathrm{m}$ and $d = 12\,\mu\mathrm{m}$ (dotted line); (c) Recruitment rate for $\Delta|\tilde{\mathbf{E}}|$=0 %/mm derived from the individual neuron activation in (b) by integrating over the electric field thresholds. The dashed line indicates the electric field intensity where the recruitment rate is 0.5.

370   ### 3.2.2 Nested Basket cells

371   The results of the average response model of L4 NBCs in case of a monophasic excitation is shown in

372   Fig. 7. Their axonal arborization is distinct from pyramidal cells because they form intricate networks

373   of branches that wrap around the soma of nearby pyramidal cells, forming a characteristic "basket"

374   structure. Their axonal structure is generally more isotropic compared to pyramidal cells or SBCs and

375   LBCs. Nevertheless, the thresholds for tangential electric fields are about 14% higher compared to

376   normal electric fields (ϑ=0° and ϑ=180°). On average, the thresholds of L4 NBCs are 2% and 23% higher

377   compared to L2/3 PCs and L5 PCs, respectively. The results for biphasic excitation are shown in Fig S3
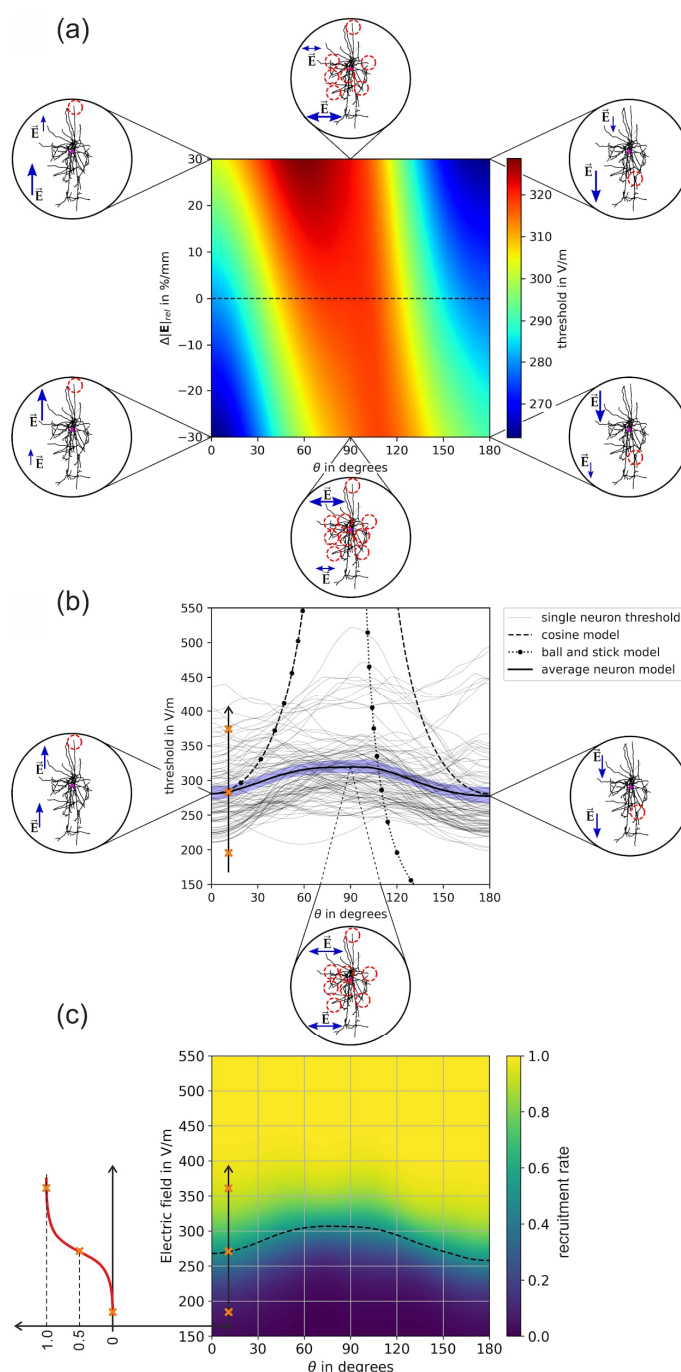
378   in the *Supplemental Material*.

Figure 7: Stimulation behavior of L4 NBCs for monophasic excitation: (a) Threshold map in dependence of the polar angle ϑ and the relative change of the electric field over the somato-dendritic axis $\Delta|\tilde{\mathbf{E}}|$. The insets show the locations of excitation, the red circles indicate the activated terminals. Blue arrows indicate the electric field direction and magnitude; (b) Thresholds of individual neurons for $\Delta|\tilde{\mathbf{E}}|$=0 %/mm along the dashed line in (a). The blue area shows the 95th percentile of the confidence interval of the mean. The equivalent cortical column cosine model is $y(\theta) = \hat{y}|\cos(\theta)|^{-1}$ with $\hat{y}$=178.43 V/m (dashed line); the axon parameters of the equivalent ball-and-stick model are $l = 560\,\mu\mathrm{m}$ and $d = 11\,\mu\mathrm{m}$ (dotted line); (c) Recruitment rate for $\Delta|\tilde{\mathbf{E}}|$=0 %/mm derived from the individual neuron activation in (b) by integrating over the electric field thresholds. The dashed line indicates the electric field intensity where the recruitment rate is 0.5.

21

3.2.3 Large Basket cells

The threshold results of L4 LBCs for monophasic excitation are shown in Fig. 8. Compared to PCs, LBCs exhibit a high degree of collateralization in their axonal tree. They can have multiple branches and collaterals that extend in different directions within the same cortical layer or across layers. A distinct directional sensitivity of the thresholds can be again observed together with an asymmetric modulation when the electric field changes along the somato-dendritic axis. On average, the thresholds of L4 LBCs are 9% lower than L2/3 PCs and 11% higher compared to L5 PC, respectively. Of all the basket cells investigated, the LBCs have the lowest thresholds. The average thresholds of LBCs are 24% and 10% lower compared to SBCs and NBCs, respectively. The results for biphasic excitation are shown in Fig S4 in the *Supplemental Material*.
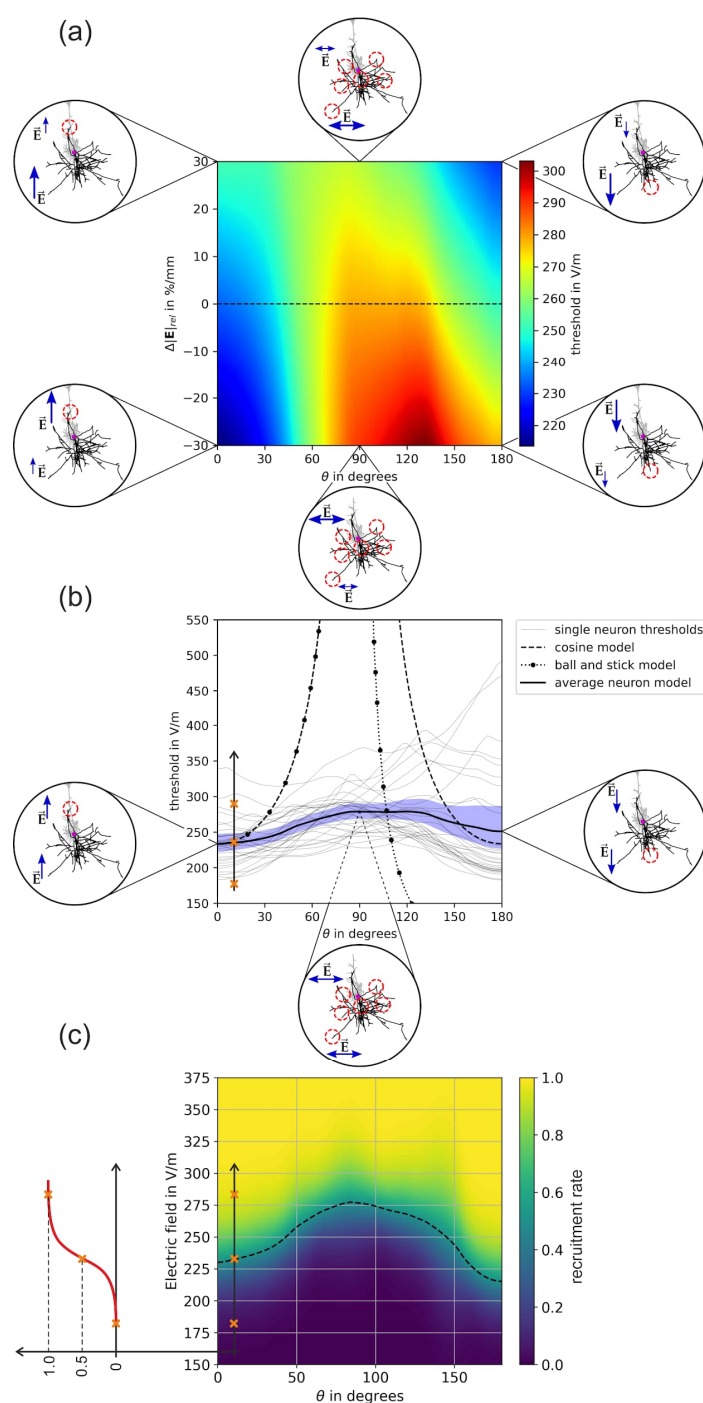
400

Figure 8: Stimulation behavior of L4 LBCs for monophasic excitation: (a) Threshold map in dependence of the polar angle ϑ and the relative change of the electric field over the somato-dendritic axis $\Delta|\tilde{\mathbf{E}}|$. The insets show the locations of excitation, the red circles indicate the activated terminals. Blue arrows indicate the electric field direction and magnitude; (b) Thresholds of individual neurons for $\Delta|\tilde{\mathbf{E}}|$=0 %/mm along the dashed line in (a). The blue area shows the 95th percentile of the confidence interval of the mean. The equivalent cortical column cosine model is $y(\theta) = \hat{y}|\cos(\theta)|^{-1}$ with ŷ=178.43 V/m (dashed line); the axon parameters of the equivalent ball-and-stick model are $l = 620\,\mu\mathrm{m}$ and $d = 15\,\mu\mathrm{m}$ (dotted line); (c) Recruitment rate for $\Delta|\tilde{\mathbf{E}}|$=0 %/mm derived from the individual neuron activation in (b) by integrating over the electric field thresholds. The dashed line indicates the electric field intensity where the recruitment rate is 0.5.

23

3.3 Stimulation behavior of L5 PCs

The stimulation behavior for L5 PCs in case of monophasic excitation is shown in Fig. 9. Coto the behavior of the other cell types investigated, the L5 PCs have the lowest average thresholds (Fig 9a). The thresholds for tangential electric fields (ϑ=90°) are about 15% higher compared to normal electric fields (ϑ=0° and ϑ=180°). The results of the individual neurons in Fig. 9b show that the variance of the thresholds increases with increasing ϑ. At ϑ=180°, a cluster of neurons can be identified that have very low stimulation thresholds. These are paralleled by a few neurons that have very high stimulation thresholds compared to this group. This affects the recruitment rate in Fig. 9c, whose 50% level (dashed line) is lower at ϑ=180° than at ϑ=0°. The most efficient way to stimulate L5 PCs is the application of electric fields with a polar angle of ϑ=0° and a negative change in electric field across the somato-dendritic axis ($\Delta|\tilde{\mathbf{E}}|<0$) or by applying electric fields with an angle of ϑ=180° together with a positive field change ($\Delta|\tilde{\mathbf{E}}|>0$). For ϑ=180° the stimulation locations are at the lower axons indicating a tendency for cortico-spinal activation. In contrast, when the electric field is antidromic at ϑ=0°, axon collaterals in the upper part are preferentially stimulated, indicating cortico-cortical activation of, for example, connected populations of L2/3 PCs. The stimulation behavior is much more diverse for transverse electric fields around ϑ≈90° due to the variety of azimuthal angles φ in which cortico-cortical and cortico-spinal connections can be stimulated. The results for biphasic excitation are shown in Fig S5 in the *Supplemental Material*.

429

Figure 9: Stimulation behavior of L5 PCs for monophasic excitation: (a) Threshold map in dependence of the polar angle ϑ and the relative change of the electric field over the somato-dendritic axis $\Delta|\tilde{\mathbf{E}}|$. The insets show the locations of excitation, the red circles indicate the activated terminals. Blue arrows indicate the electric field direction and magnitude; (b) Thresholds of individual neurons for $\Delta|\tilde{\mathbf{E}}|$=0 %/mm along the dashed line in (a). The blue area shows the 95th percentile of the confidence interval of the mean. The equivalent cortical column cosine model is $y(\theta) = \hat{y}|\cos(\theta)|^{-1}$ with ŷ=233.66 V/m (dashed line); the axon parameters of the equivalent ball-and-stick model are $l = 760\,\mu\mathrm{m}$ and $d = 15\,\mu\mathrm{m}$ (dotted line); (c) Recruitment rate for $\Delta|\tilde{\mathbf{E}}|$=0 %/mm derived from the individual neuron activation in (b) by integrating over the electric field thresholds. The dashed line indicates the electric field intensity where the recruitment rate is 0.5.

25

440   3.4 Recruitment order and relative threshold ranges

441   For each cell type investigated, different stimulation thresholds were observed depending on the polar

442   angle ϑ and the relative change of the electric field over the somato-dendritic axis $\Delta|\tilde{\mathbf{E}}|$. In Fig. 10, an

443   overview of the threshold ranges of all investigated cell types relative to the mean of L5 PCs, is shown,

444   assuming a constant electric field along the somatodendritic axis ($\Delta|\tilde{\mathbf{E}}|$=0 %/mm). It is evident that L5

445   PCs are recruited first due to their relatively low thresholds. The L4 LBCs have the second lowest

446   thresholds followed by the L2/3 PCs and the L4 NBCs. The small basket cells are directly stimulated

447   only at higher stimulation intensities. An analogous observation was also made for biphasic TMS pulses

448   and the results are reported in Fig. S6 in the *Supplemental Material.*
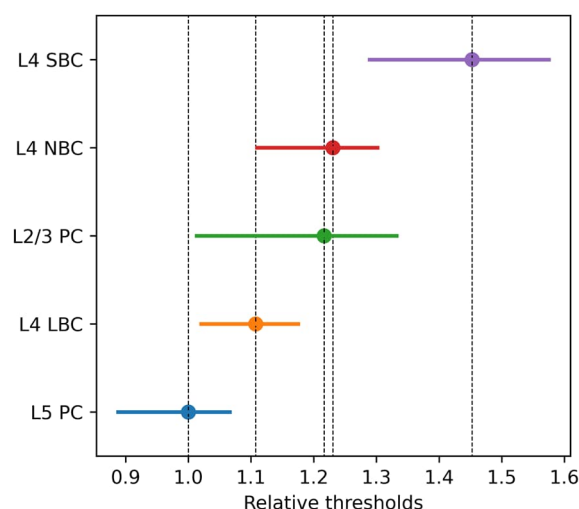

449

450   Figure 10: Recruitment order and relative threshold ranges of pyramidal and basket cells for
451   monophasic TMS excitation: Threshold ranges of all investigated cell types relative to the mean of L5
452   PCs, is shown assuming a constant electric field along the somatodendritic axis ($\Delta|\tilde{\mathbf{E}}|$=0 %/mm). The
453   dots indicate the mean thresholds and the ranges stem from the variability across the polar angle ϑ
454   from 0° to 180°.

455   3.5 Sensitivity analysis

456   We used a 15th order approximation to construct the surrogate models of the threshold maps using

457   *pygpc* (Weise et al., 2020b). The normalized root mean square deviation between the original model

458   and the gPC approximation is 0.32% for L5 PC under monophasic excitation derived from 10^5 random

459   samples. The accuracies of the gPC approximations of the L2/3 and L4 cells are very similar and given

26

460   in the repository by Weise et al. (2023b). The results of the sensitivity analysis of the threshold map of

461   L5 PC with monophasic excitation is shown in Fig. 11. It can be seen that the surrogate model (Fig. 11b)

462   almost perfectly resembles the behavior of the original model (Fig. 11a). The absolute differences

463   between both is shown in Fig. 11c. The probability density distribution of the electric field threshold is

464   shown in Fig. 11d under the assumption that the parameters ϑ and $\Delta|\tilde{E}|$ are beta distributed as in case

465   of the realistic head model simulations (see Fig. 3 for parameter values). It can be observed that the

466   distribution is u-shaped and bimodal because of the cyclic behavior of the electric field threshold over

467   the polar angle ϑ. The results for L5 in case of monophasic excitation as well as for L2/3 PC, and L4

468   S/N/LBC for both monophasic and biphasic excitation are given in the repository Weise et al. (2023b).

469   The Sobol indices, i.e. the fractions of the total variance, which originate from ϑ, $\Delta|\tilde{E}|$, and the

470   combination of both are given in Table 1. The polar angle ϑ has the strongest influence on the

471   stimulation behavior for all investigated cell types. In contrast, the Sobol indices of $\Delta|\tilde{E}|$ are much

472   lower, ranging between 2-5%, but the parameter significantly contributes to the increase of the

473   accuracy of the overall model. There is even an exception in the L2/3 cells under biphasic excitation,

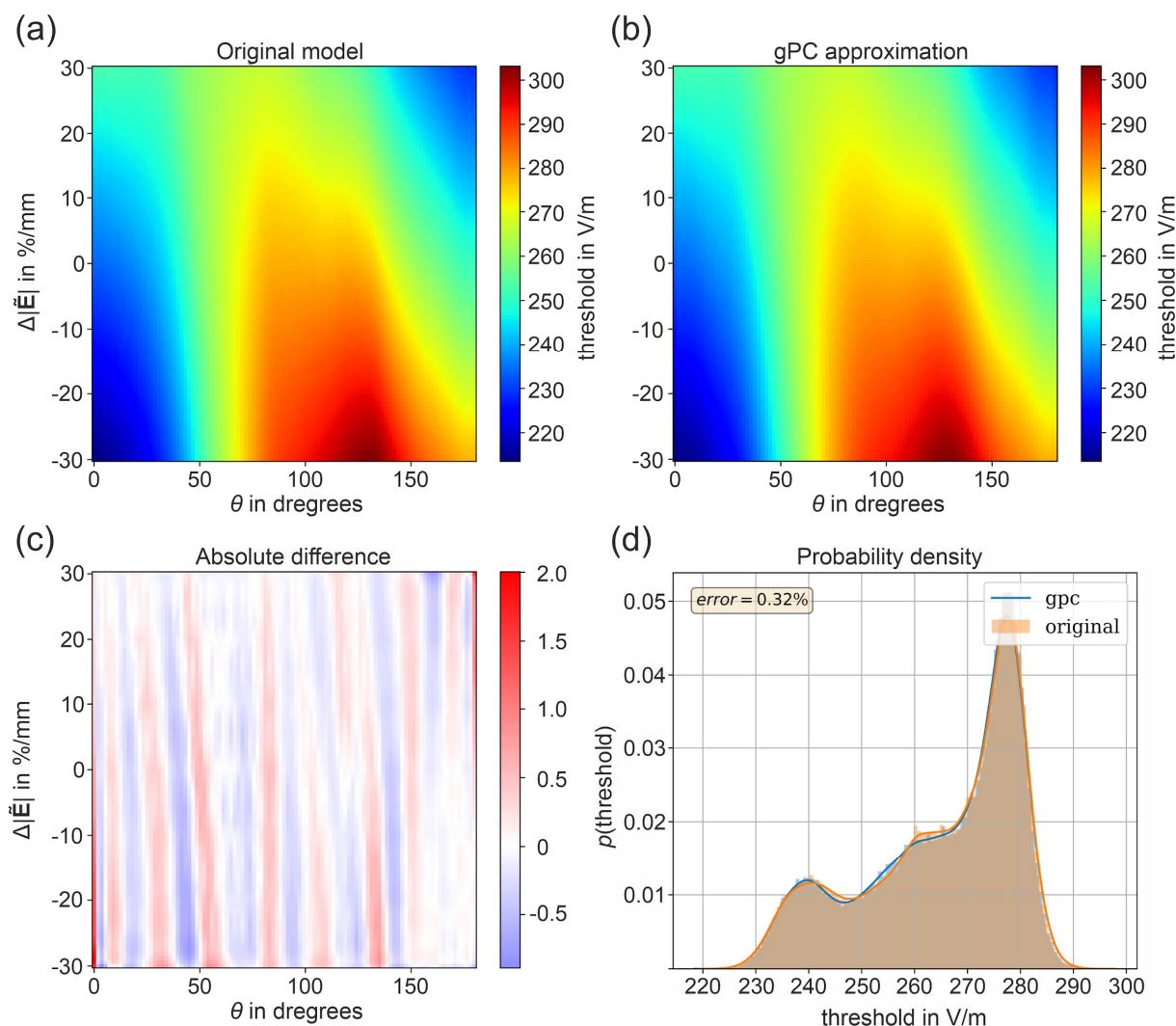474   where the influence reaches almost 25%.

Figure 11: Results of the sensitivity analysis of the electric field threshold map of L5 PCs with monophasic excitation: (a) Original model of the threshold map of L5 PC with monophasic excitation; (b) gPC approximation (surrogate) of the original model; (c) Absolute difference between the original model and the gPC approximation; (d) Probability density of the electric field threshold for the original model and the gPC approximation using $N=10^5$ samples under the assumption that ϑ and $\Delta|\tilde{\mathbf{E}}|$ are beta distributed (see Fig. 3 for parameters).

Table 1: Sobol indices of the electric field threshold models for L2/3, L4 S/N/LBC, and L5 PC for monophasic and biphasic pulse waveforms.

Cell type	L2/3 PC		L4 SBC		L4 NBC		L4 LBC		L5 PC	
wave-form	mono-phasic	bi-phasic	mono-phasic	bi-phasic	mono-phasic	bi-phasic	mono-phasic	bi-phasic	mono-phasic	bi-phasic
ϑ	0.919	0.710	0.991	0.994	0.974	0.985	0.962	0.974	0.951	0.971

28

$\Delta\lvert\tilde{\boldsymbol{E}}\rvert$	0.052	0.247	0.001	0.001	0.001	0.001	0.003	0.002	0.037	0.017
ϑ & $\Delta\lvert\tilde{\boldsymbol{E}}\rvert$	0.029	0.043	0.008	0.005	0.025	0.014	0.035	0.024	0.012	0.012

485

3.6 Verification

The average threshold model is compared against reference simulations using a high resolution realistic head model. For the application of the average model, we extracted the electric field parameters ϑ and $\Delta\lvert\tilde{\boldsymbol{E}}\rvert$ in every cortical element in the ROI on layer 2/3, 4, and 5 and determined the electric field thresholds (Fig. 5-9) by linearly interpolating the data between the sampling points. The approach is computationally very efficient, as the computation time is only a fraction of the one needed for the electric field computation. In the reference simulations, we calculated the stimulation thresholds for every neuron at every cortical location in the ROI separately by coupling the actual electric fields from the realistic head model into every neural compartment. Finally we averaged the thresholds over all neurons and assigned the resulting average threshold to the ROI element. The resulting electric field threshold maps between the average threshold model and the reference simulations are shown in Fig. 12 for all cell types under investigation. The results for biphasic excitation are shown in Figure S8 in the *Supplemental Material*.

For all stimulation conditions, the two models agree very well. The highest relative differences are in the range of ±8% and can be observed mainly at the gyral rims and the sulcal walls. Comparing the distributions and signs of the relative differences between monophasic and biphasic waveforms, it can be observed that they slightly depend on the stimulation waveform and the resulting current direction.
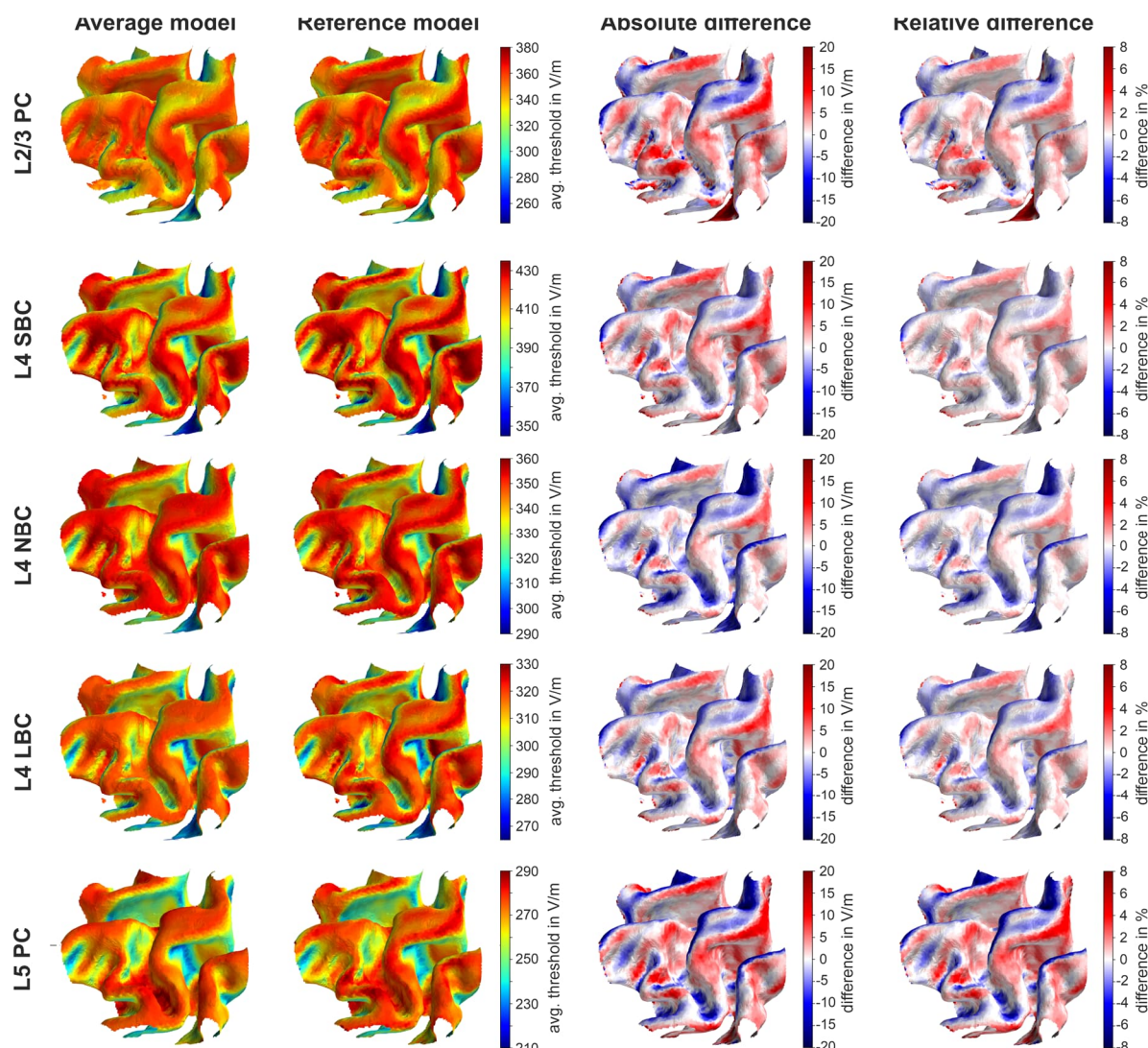
Figure 12: Comparison of electric field threshold maps (in V/m) for monophasic excitation determined using the average model and the reference model: The rows show the electric field threshold maps (in V/m) of the L2/3 PC, L4 S/N/LBC and the L5 PC between the average model (first column) and the reference model (second column). The last two columns show the absolute and relative difference between the models. The underlying electric field distribution and field direction is shown in Fig. 4. The results for biphasic excitation are shown in Figure S8.

Additionally, we calculated the stimulation threshold maps when the TMS coil is located over the M1 region with a 45° orientation towards the *fissura longitudinalis*. For this, we determined the ratio between the electric field threshold map from Fig. 12 and the corresponding electric field distribution of this particular coil position, which was calculated assuming a normalized stimulation strength of 1 A/µs. This results in a map of the stimulation strength of the TMS stimulator in A/µs needed to stimulate the neurons with this particular coil position. Again a high agreement between the average threshold model and the reference model can be observed. Note that the relative difference

30

518   distributions in the last column of Fig. 13 are the same as for the electric field threshold maps from Fig.

519   12 since the electric field distribution is cut out in the error calculation. The analogous results for

520   biphasic excitation are shown in Fig. S9.

521

522
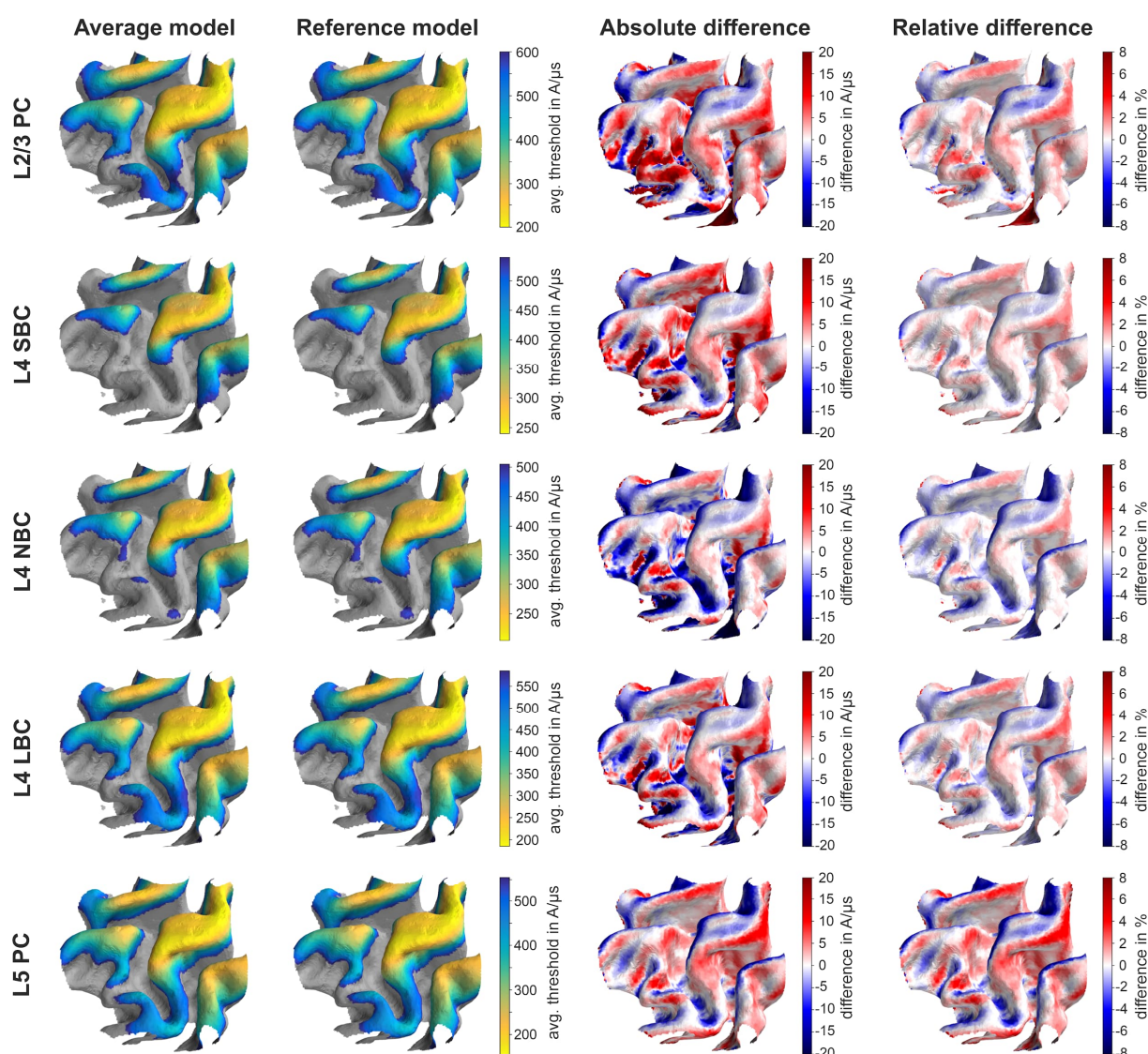
Figure 13: Comparison of stimulation intensity threshold maps (in A/µs) for monophasic excitation determined using the average model and the reference model: The first two rows show the stimulation threshold maps (in A/µs) of the L2/3 PC and the last two rows of the L5 PC between the average model (first column) and the reference model (second column). The last two columns show the absolute and relative difference between the models. It is assumed that the TMS coil is located over the M1 area with an orientation of 45° towards the *fissura longitudinalis*. The maps indicate the stimulation strength of the TMS device in A/µs, which is required to stimulate this cortical area for this particular coil position and orientation. The underlying electric field distribution and field direction is shown in Fig. 4. The results for biphasic excitation are shown in Figure S9.

532   To quantify the differences between the models, we determined the normalized root mean square

533   error (NRMSE):

$$\text{NRMSE} = \sqrt{\frac{\sum_{i=1}^{N_{ROI}}\left(y_{i,ref} - y_i\right)^2}{\sum_{i=1}^{N_{ROI}} y_{i,ref}^2}}$$

534   (3)

535   where $y_{i,\,ref}$ denotes the thresholds of the reference simulations in the i-th ROI element and y_i the

536   thresholds from the average model. Additionally, we calculated the mean absolute percentage error

537   (MAPE) quantifying the prediction accuracy of the average models:

$$\text{MAPE} = \frac{1}{N_{ROI}} \sum_{i=1}^{N_{ROI}} \left| \frac{y_{i,ref} - y_i}{y_{i,ref}} \right|$$

538   (4)

539   and the coefficient of determination (R^2) quantifying the proportion of the total variance explained by

540   the average model:

$$R^2 = 1 - \frac{\sum_{i=1}^{N_{ROI}}\left(y_i - y_{i,ref}\right)^2}{\sum_{i=1}^{N_{ROI}}\left(y_i - \bar{y}\right)^2}$$

541   (5)

542   where $\bar{y}$ is the mean of the average threshold model.

543   The histograms of the relative differences are shown in Fig. 14 together with the different error

544   measures. The distribution of relative differences is relatively symmetric and the means are close to

545   zero. The remaining variance results from the inhomogeneity of the electric field across the neurons.

546   Systematic field distortions in a particular direction across neurons, such as those occurring at the gyral

547   crowns, are neglected and result in deviations from the exact reference model because in the

548   simplified model, only the decay of the electric field across the somatodendritic axis can be accounted

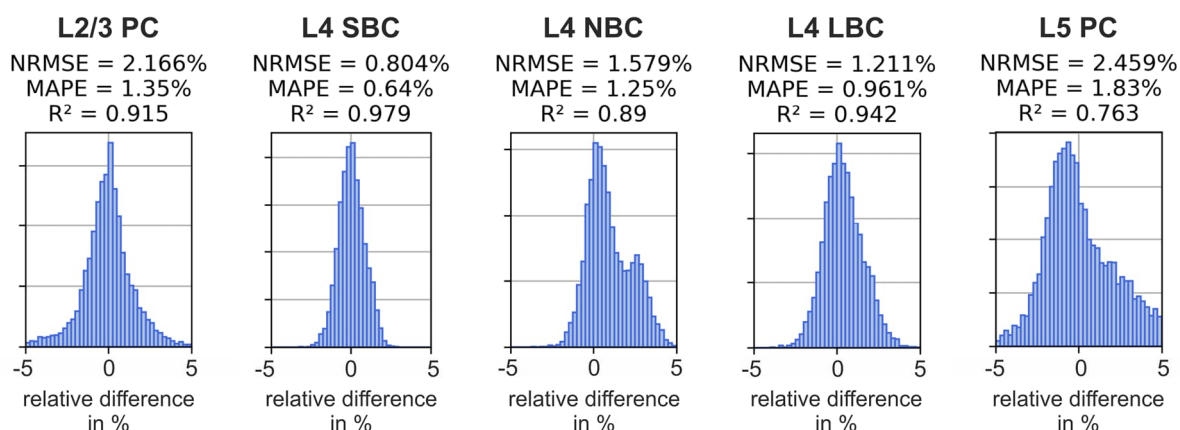549   for due to averaging over the azimuthal angle.

Figure 14: Differences of the threshold maps between the average model and the reference model for monophasic excitation. Histograms of the relative difference between the reference model and the average threshold model over the ROI elements. Normalized root mean square error (NRMSE), mean absolute percentage error (MAPE), and coefficient of determination (R^2) for L2/3 PC and L5 PC with monophasic and biphasic excitation. The results for biphasic excitation are shown in Fig. S10.

3.7 Validation

The predicted orientation sensitivity of the neurons is compared to the orientation sensitivity of MEPs. The polar plot in Fig. 15 shows the MEP amplitudes for different electric field angles and stimulation intensities together with the predictions of the recruitment rate from the average threshold model from L5 PC under monophasic excitation. To make both representations comparable, the data were normalized to their respective maximum values. The average threshold model closely matches the orientation sensitivity of MEPs and the NRMSE between the experimental data and model predictions is 8.5%. It can be clearly observed that the directional sensitivity is more pronounced for low stimulation intensities close to rMT than for higher ones. The cortical column cosine model resembles the general behavior of the directional sensitivity of the MEPs at low stimulation intensities, but cannot represent the stimulation behavior in the transition to higher stimulation intensities. The ball-and-stick model was also not able to reflect the direction sensitivity over the investigated parameter range for both the incident angle ϑ and the stimulation intensity.
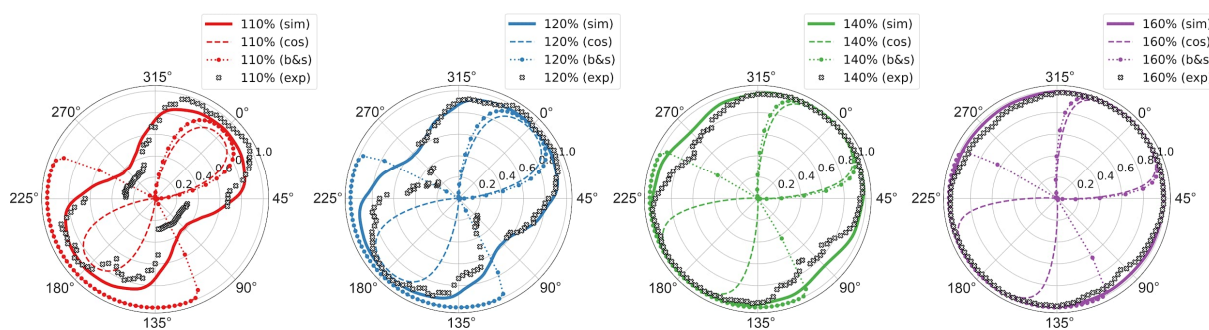
Figure 15: Comparison between directional sensitivity of motor evoked potentials and the derived recruitment rate from the theoretical neuronal response model: The plots show the directional sensitivity of measured MEPs as black crosses (exp) at different stimulation intensities with respect to resting motor threshold of subject 16 from Souza et al. (2022). The solid lines (sim) show the corresponding trajectory of the recruitment rate along ϑ assuming a constant electric field along the somato-dendritic axis ($\Delta|\tilde{\mathbf{E}}|$=0 %/mm), and the dashed and the dotted lines show the predictions of the directional sensitivity of the MEPs according to the cortical column cosine model (cos) and the ball-and-stick model (b&s). The MEPs were normalized to their maximum values for comparability. The NRMSE between the experimental data and the recruitment rate model (sim) is 8.5%.

4 Discussion

In order to link the predicted electric field to actual neural activation, a range of different proposals with varying degrees of complexity have been put forward. The simplest approach just considers the magnitude of the electric field as a proxy for the activation strength (e.g., Weise et al., 2021), without any dependency on direction or local gradient of the field. This method disregards experimental observations and theoretical considerations showing that the activation threshold does indeed depend on the incidence angle between the field direction and the orientation of the axons (Rushton, 1927; Rudin and Eisenman, 1954; Ranck, 1975). This consideration led to the proposal of the cortical column cosine model (Fox et al., 2004), which is based on the assumption that axons aligned with the somato-dendritic axis (i.e., perpendicular to the cortical surface) dominate the stimulation process, and

589 therefore predicts that only the projection of the electric field onto that axis has an effect. As a

590 consequence, purely tangential fields would lead to no stimulation.

591 However, it is known that the axonal arbors of cortical cells are much branched and cover all directions

592 (Aberra et al., 2020). In line with this, in earlier TMS motor mapping experiments (Weise et al., 2020,

593 Numssen et al., 2021, Weise et al., 2023a), we could show that the tangential field component does

594 indeed have a substantial predictive power towards the resulting motor evoked potentials. In fact, it

595 was even considerably more powerful than the radial component (i.e., the one aligned with the

596 somato-dendritic axis), which can be understood in the light of the cortical geometry: At the gyral

597 crowns, the field is largely tangential to the cortical surface (thus, having less impact), but its

598 magnitude is much larger due to the greater proximity to the coil, thus overcompensating the former

599 effect. In contrast, at the sulcal walls, located more distant to the coil, the field is radial, but much

600 weaker, and therefore often does not effectively stimulate.

601 In order to obtain a more accurate account of the coupling between the electric field and the activation

602 states of cortical neurons, detailed biological models based on realistic neuronal geometry and realistic

603 Hodgkin-Huxley-like neural dynamics have been proposed (Aberra et al., 2018, 2020). These models

604 have the potential to deliver a detailed and accurate picture of neuronal activation by TMS. However,

605 they are computationally extremely demanding and therefore hardly suitable for routine applications,

606 such as mapping or dosing. Moreover, the utilized neural geometries must be considered as samples

607 of a distribution and do not account for any precise individual cortical architecture. This suggests that

608 the predictions of these models should be representable in low-parametric models without much loss.

609 In our study, we attempt to bridge the gap between, on the one hand, the imprecise oversimplification

610 of the magnitude, cortical column cosine, and ball-and-stick models and, on the other hand, the

611 unwieldy and time-consuming biologically realistic modeling. The model we propose is as easily

612 applicable as the former, while it very closely approximates the predictions of the latter. It determines

613 the stimulation thresholds as functions of field angle with respect to the somato-dendritic axis,

35

614   intensity, pulse waveform, and field decay along the somato-dendritic axis, and only requires the

615   induced electric field as an input variable. Comparison with reference simulations with a detailed

616   neuronal model yielded normalized root mean square errors of only 1.5-2.5%. It should be emphasized,

617   however, that our model is not independent, but depends, for initial calibration, on a biologically

618   realistic model based on the principal approach of Aberra and colleagues (2018, 2020).

619   Our model predicts a certain dependence of the stimulation threshold on the angle of incidence of the

620   electric field, which is more pronounced for monophasic pulses than for biphasic pulses. However,

621   compared to the predictions from simplified models such as the cortical column cosine model or ball-

622   and-stick neurons, this dependence is much more moderate. This allows tangential electric fields of

623   sufficient strength to contribute to the stimulation, as has been observed in previous experimental

624   studies (Weise et al., 2020, Numssen et al., 2021). In particular, the L2/3 PC require 108%, L4 SBC

625   require 113%, L4 NBC require 110%, L4 LBC require 114%, and L5 PC require 120% of the longitudinal

626   stimulation strength (ϑ=0°) at ϑ=90° for monophasic excitation, respectively. For a comparison of the

627   directional sensitivity profiles of our model and the cortical column cosine and ball-and-stick models,

628   see Fig. 5-9.

629   These findings are confirmed by a comparison to the experimentally observed orientation sensitivity

630   of MEPs (Fig. 14), where a difference of only 8.5% was observed between model predictions and

631   experimental data. We observed a high directional sensitivity at low stimulation intensities close to

632   the motor threshold, while at higher stimulation intensities the directional sensitivity rapidly

633   decreases. While our model appears to be a quite good predictor of the directional sensitivity

634   observed by Souza et al. (2022), there are also deviations. This is mainly explainable in the light of some

635   important discrepancies between the assumptions underlying our model and those made by these

636   authors. First, the results of Souza and colleagues are based on electric fields predicted using a

637   spherical head model, while our model works with a realistic head model. Second, Souza's report is

638   based on the electric field direction with respect to the global coordinate system, while our angle

639   definition is local and changes across the strongly curved cortical surface. Third, the location of the

640 neuronal populations that mediate the relationship between stimulation and MEP is only roughly

641 known in Souza et al. (2022). It may therefore be that the field angles at that location are different

642 from those predicted for the assumed target spot. Accordingly, for an even better comparison, the

643 currents in the multi-coil array would have to be optimized subject- and target-specifically to realize

644 an ideal rotation of the electric field at a constant field strength in the target. This in turn requires

645 precise knowledge of the target and thus a prior mapping of the motor cortex such as in Weise et al.

646 (2023a).

647 The major advantage of the presented model is its simplicity without sacrifice of realism. The

648 availability of look-up tables of threshold maps and recruitment rates allows for the simple

649 construction of interpolators and functions for computation. Alternatively, polynomial-based

650 surrogate models based on generalized polynomial chaos (gPC; Weise et al., 2020b) can be used for

651 this purpose and provide high accuracy. Examples are given in the repository of Weise et al. (2023b).

652 Importantly, the model is easy to adapt and refine, if more or better information about the neuronal

653 geometry of particular tissues becomes available, using the provided scripts and simulation code

654 (https://github.com/TorgeW/TMS-Neuro-Sim). Already in this study, we were able to distinguish

655 between the stimulation thresholds and distributions among various distinct cell types. We observed

656 that L5 PCs had the lowest thresholds compared to all other cell types studied, followed by L4 LBC and

657 L2/3 PCs, which had 10% and 22% higher thresholds, respectively. This "library" of cellular stimulation

658 profiles may be extended in the future. By comparison with experimentally observed stimulation

659 profiles, such cell-specific sensitivity profiles may potentially allow for testing hypotheses about which

660 cells are actually stimulated in particular experimental situations.

661 These traits allow for efficient implementation and extension of TMS models in the context of

662 optimization, mapping, and dosing without the need to implement time consuming and complicated

663 neuron models. Especially in the field of cognitive TMS experiments, where an adequate dosing

664 strategy is still subject to research, the gained knowledge could significantly contribute to the

665   identification of the effectively stimulated regions but also to exclude regions that are not eligible for

666   stimulation due to the underlying electric field distribution and orientation relative to the cortex.

667   The threshold maps have revealed interesting parameter combinations of ϑ and $\Delta|\tilde{\mathbf{E}}|$ that enable

668   particularly effective stimulation. Here, an interesting observation is that an increase of the electric

669   field along the somato-dendritic axis of the neurons ($\Delta|\tilde{\mathbf{E}}|>0$) from the GM surface to the WM surface

670   is as likely as a decrease and is usually in the range of $\pm20\%$/mm (Fig. 3b). Future optimization studies

671   could be directed towards identifying coil positions and orientations that realize these parameter

672   combinations in the targeted region. As a result, such new optimization strategies would have great

673   potential to significantly enhance the overall efficacy of TMS and reduce the required dose. At the

674   same time, the optimization criterion can be extended such that the electric field is oriented to *prevent*

675   stimulation of other brain regions by targeting particularly high thresholds. This principled approach

676   of multi-objective optimization was also taken up by Lueckel et al. (2022) in the framework of electric

677   field and connectivity optimized TMS targeting.

678   Another area of application for the presented models is in the extension of existing mapping

679   procedures (Weise et al., 2020, Numssen et al., 2021; Weise et al., 2023a), as mentioned previously.

680   Instead of the electric field magnitude, some kind of effective electric field could be used as a regressor

681   for localization. It is noted that the integration of the stimulation thresholds into the analysis

682   procedures occurs solely at the modeling level, thus improving the efficiency of the mapping

683   procedures without increasing the experimental effort. Stronger even, the fact that we have an

684   estimate of the stimulation threshold at every cortical location, we can successively exclude locations

685   which are stimulated without an observable effect (e.g., MEP), and thereby even decreasing the

686   experimental effort.

687   Limitations of the study

688   The number of L2/3 and L5 neurons available was limited. We were able to significantly expand the

689   original dataset of Aberra et al. (2018) and Aberra et al. (2020), but especially for the calculation of the

690   recruitment rate, a higher number of neurons would increase the model accuracy.   This is especially

691   true for incident angles where threshold variances are high.

692   Moreover, we limited the analysis to pyramidal cells in L2/3, L5, and Basket cells in L4, which take a

693   major part in generalized cortical circuits (Di Lazzaro et al., 2012). However, it is known that other cell

694   types like spiny stellates in L4, also play a major role in the stimulation of cortical microcircuits. The

695   development of average threshold models for other cell types is straightforward using the tools

696   provided in the repository Weise et al. (2023b) and the Python package *TMS-Neuro-Sim*

697   (https://github.com/TorgeW/TMS-Neuro-Sim) if the appropriate morphologies and parameterizations

698   are available.

699   In the modeling, we also neglected the effect of the presence of the neurons and other cells to the

700   external electric field. While for the macroscopic field estimation, these structures are already

701   accounted for through the (macroscopically acquired) tissue conductivity, at the microscale, the

702   presence of low conducting membranes might cause local deviations from that macroscopically

703   predicted field, which may have an effect on the actual stimulation of neurons.

704   Future work

705   Insights into the stimulation behavior of neurons are essential to develop realistic coupling models for

706   downstream neuronal mass models along the lines of Montbrió et al. (2015) or Jansen and Rit (1995),

707   which in turn could be used to model the dynamic processes of entire populations of neurons, such as

708   the D- and I-wave dynamics in the motor cortex (Di Lazzaro et al. 1998, ; Di Lazzaro et al., 2012;

709   Ziemann, 2020).

710   In further follow-up studies, the degree to which the spatial fine-structure of the electric field is

711   affected by the high membrane resistance of the neurons should be investigated. The resulting change

712   in the electric field distribution may have a non-negligible influence on the local electric field angles

713   and magnitudes, which in turn change the stimulation thresholds. However, this will require very

714   detailed volume conductor models of whole cortical columns or at least geometric information about

715   the neuron surfaces and their position with respect to each other. It is expected that this type of model

716   will require high computational power to solve and is far from being routinely used in daily TMS

717   experiments and that it will lead to an anisotropic macroscopic conductivity profile as well as

718   potentially modified sensitivity profile due to local electric field fluctuations. The former can be

719   estimated with diffusion-weighted MRI (Güllmar et al., 2010), but its influence on the stimulation

720   behavior on a micro- and mesoscopic scale is yet unknown. The goal of such a study could be the

721   derivation of a new generation of low-parametric models, in a similar sense as in this study, in order

722   to be able to apply the gained knowledge in practice.

723   A further step towards a more accurate biophysical modeling of the stimulation processes may consist

724   in the consideration of the back reaction of the neurons to the extracellular potential when action

725   potentials are generated. Active ion transport alters the total electric field and can lead to mutual

726   interference (cross-talk) between neurons. For such a model, the neurons can no longer be considered

727   separately, but must be simulated as a unit in the form of a cortical column or similar. Such a model

728   approach can be combined with the previous one, but it is expected that the required computing time

729   will be even higher to solve it.

Acknowledgements

Conflicts of interest

The authors declare that they have no known competing financial interests or personal relationships that could have appeared to influence the work reported in this paper.

References

Aberra, A. S., Peterchev, A. V., Grill, W. M. (2018). Biophysically realistic neuron models for simulation of cortical stimulation. *Journal of neural engineering*, *15*(6), 066023.

Aberra, A. S., Wang, B., Grill, W. M., Peterchev, A. V. (2020). Simulation of transcranial magnetic stimulation in head model with morphologically-realistic cortical neurons. *Brain stimulation*, *13*(1), 175-189.

Anwar, H., Riachi, I., Hill, S., Schurmann, F., & Markram, H. (2009). An approach to capturing neuron morphology diversity. *Computational neuroscience: Realistic modeling for experimentalists*, 211-232. doi: 10.7551/mitpress/9780262013277.003.0010

Aspart, F., Ladenbauer, J., & Obermayer, K. (2016). Extending integrate-and-fire model neurons to account for the effects of weak electric fields and input filtering mediated by the dendrite. *PLoS computational biology*, *12*(11), e1005206.

Bédard, C., & Destexhe, A. (2008). A modified cable formalism for modeling neuronal membranes at high frequencies. Biophysical journal, 94(4), 1133-1143.

Dale, A. M., Fischl, B., & Sereno, M. I. (1999). Cortical surface-based analysis: I. Segmentation and surface reconstruction. *Neuroimage*, *9*(2), 179-194.

Di Lazzaro, V., Profice, P., Ranieri, F., Capone, F., Dileone, M., Oliviero, A., & Pilato, F. (2012). I-wave origin and modulation. Brain stimulation, 5(4), 512-525.

758 Di Lazzaro, V. D., Restuccia, D., Oliviero, A., Profice, P., Ferrara, L., Insola, A., ... & Rothwell, J. (1998).
759 Effects of voluntary contraction on descending volleys evoked by transcranial stimulation in conscious
760 humans. The Journal of physiology, 508(2), 625-633.

761 Fischl, B., Dale, A. M., Sereno, M. I., Tootell, R. B. H., Rosen, B. R. (1998). A coordinate system for the
762 cortical surface. *NeuroImage*, *7*(4), S740.

763 Fox, P. T., Narayana, S., Tandon, N., Sandoval, H., Fox, S. P., Kochunov, P., & Lancaster, J. L. (2004).
764 Column-based model of electric field excitation of cerebral cortex. *Human brain mapping*, *22*(1), 1-14.

765 García-Cabezas, M. Á., Barbas, H. (2014). Area 4 has layer IV in adult primates. *European Journal of*
766 *Neuroscience*, *39*(11), 1824-1834.

767 Gaser, C., Dahnke, R., Thompson, P. M., Kurth, F., Luders, E. (2022). CAT-a computational anatomy
768 toolbox for the analysis of structural MRI data. *BioRxiv*.

769 Güllmar, D., Haueisen, J., Reichenbach, J. R. (2010). Influence of anisotropic electrical conductivity in
770 white matter tissue on the EEG/MEG forward and inverse solution. A high-resolution whole head
771 simulation study. *Neuroimage*, *51*(1), 145-163.

772 Hess, A., Young, J. Z. (1949). Correlation of internodal length and fibre diameter in the central nervous
773 system. *Nature,* 164, 490–1

774 Hursh, J. B. (1939). Conduction velocity and diameter of nerve fibers. *Am. J. Physiol.,* 127, 131-139

775 Jansen, B. H., & Rit, V. G. (1995). Electroencephalogram and visual evoked potential generation in a
776 mathematical model of coupled cortical columns. *Biological cybernetics*, *73*(4), 357-366.

777 Lorensen, W. E., Cline, H. E. (1987). Marching cubes: A high resolution 3D surface construction
778 algorithm. *ACM siggraph computer graphics*, *21*(4), 163-169.

779 Lueckel, M., Radetz, A., Yuen, K., Mueller-Dahlhaus, F., Kalisch, R., & Bergmann, T. O. (2022). TU-176.
780 E-field-and connectivity-optimized TMS targeting: A pilot TMS-fMRI validation at the single-subject
781 level. *Clinical Neurophysiology*, *141*, S30-S31.

782 Markram, H., Muller, E., Ramaswamy, S., Reimann, M. W., Abdellah, M., Sanchez, C. A., ... , Schürmann,
783 F. (2015). Reconstruction and simulation of neocortical microcircuitry. *Cell*, *163*(2), 456-492.

784 Montbrió, E., Pazó, D., & Roxin, A. (2015). Macroscopic description for networks of spiking neurons.
785 *Physical Review X*, *5*(2), 021028.

786 Nicholas T. Carnevale and Michael L. Hines. The NEURON Book. Cambridge University Press, 2006. doi:
787 10.1017/CBO9780511541612.

788 Nielsen, J. D., Madsen, K. H., Puonti, O., Siebner, H. R., Bauer, C., Madsen, C. G., ... , Thielscher, A.
789 (2018). Automatic skull segmentation from MR images for realistic volume conductor models of the
790 head: Assessment of the state-of-the-art. *Neuroimage*, *174*, 587-598.

791 Numssen, O., Zier, A. L., Thielscher, A., Hartwigsen, G., Knösche, T. R., Weise, K. (2021). Efficient high-
792 resolution TMS mapping of the human motor cortex by nonlinear regression. *NeuroImage*, 245,
793 118654.

794 Penny, W. D., Friston, K. J., Ashburner, J. T., Kiebel, S. J., Nichols, T. E. (Eds.). (2011). *Statistical*
795 *parametric mapping: the analysis of functional brain images.* Elsevier.

796 Ramaswamy, S., Courcol, J. D., Abdellah, M., Adaszewski, S. R., Antille, N., Arsever, S., ... & Markram,
797 H. (2015). The neocortical microcircuit collaboration portal: a resource for rat somatosensory cortex.
798 *Frontiers in neural circuits*, 9, 44.

799 Ranck Jr, J. B. (1975). Which elements are excited in electrical stimulation of mammalian central
800 nervous system: a review. *Brain research*, 98(3), 417-440.

801 Rudin, D. O., & Eisenman, G. (1954). The action potential of spinal axons in vitro. *The Journal of General*
802 *Physiology*, *37*(4), 505-538.

803 Rushton, W. A. H. (1927). The effect upon the threshold for nervous excitation of the length of nerve
804 exposed, and the angle between current and nerve. The Journal of physiology, 63(4), 357.

805 Saturnino, G. B., Madsen, K. H., Thielscher, A. (2019). Electric field simulations for transcranial brain
806 stimulation using FEM: an efficient implementation and error analysis. *Journal of neural engineering*,
807 *16*(6), 066032.

808 Souza, V. H., Nieminen, J. O., Tugin, S., Koponen, L. M., Baffa, O., Ilmoniemi, R. J. (2022). TMS with fast
809 and accurate electronic control: Measuring the orientation sensitivity of corticomotor pathways. *Brain*
810 *Stimulation*, *15*(2), 306-315.

811 Thielscher, A., Antunes, A. and Saturnino, G.B. (2015), Field modeling for transcranial magnetic
812 stimulation: a useful tool to understand the physiological effects of TMS? IEEE EMBS 2015, Milano,
813 Italy

814 Virtanen, P., Gommers, R., Oliphant, T. E., Haberland, M., Reddy, T., Cournapeau, D., ... & Van
815 Mulbregt, P. (2020). SciPy 1.0: fundamental algorithms for scientific computing in Python. *Nature*
816 *methods*, *17*(3), 261-272.

817 Wagner, T., Gangitano, M., Romero, R., Théoret, H., Kobayashi, M., Anschel, D., ... & Pascual-Leone, A.
818 (2004). Intracranial measurement of current densities induced by transcranial magnetic stimulation in
819 the human brain. *Neuroscience letters*, *354*(2), 91-94.

820 Waxman, S. G., Kocsis, J. D. (1995). The Axon: Structure, Function, and Pathophysiology, New York:
821 Oxford University Press.

822 Weise, K., Numssen, O., Thielscher, A., Hartwigsen, G., Knösche, T. R. (2020a). A novel approach to
823 localize cortical TMS effects. *Neuroimage*, *209*, 116486.

824 Weise, K., Poßner, L., Müller, E., Gast, R., Knösche, T. R. (2020b). Pygpc: A sensitivity and uncertainty
825 analysis toolbox for Python. *SoftwareX*, *11*, 100450.

826 Weise, K., Numssen, O., Kalloch, B., Zier, A. L., Thielscher, A., Haueisen, J., Hartwigsen, G., Knösche, T.
827 R. (2023a). Precise motor mapping with transcranial magnetic stimulation. *Nature protocols*, *18*(2),
828 293-318.

829 Weise, K., Worbs, T., Kalloch, B., Thielscher, A., Knösche, T. R. (2023b). Direction Sensitivity of Cortical
830 Neurons Towards TMS Induced Electric Fields - data and code. *osf.io*,
831 https://doi.org/10.17605/OSF.IO/C8J35

832 Ziemann, U. (2020). I-waves in motor cortex revisited. Experimental Brain Research, 238(7), 1601-
833 1610.

834 Zienkiewicz, O. C., Zhu, J. (1992). The superconvergent patch recovery (SPR) and adaptive finite
835 element refinement. *Computer Methods in Applied Mechanics and Engineering, 101*(1-3), 207-224.